

Zircon Survival, Rebirth and Recycling during Crustal Melting, Magma Crystallization, and Mixing Based on Numerical Modelling

Ilya N. Bindeman^{1*} and Oleg E. Melnik^{1,2}

¹Department of Geological Sciences, University of Oregon, Eugene, OR 97405, USA; ²Institute of Mechanics, Moscow State University, Moscow, Russia

*Corresponding author. E-mail: Bindeman@uoregon.edu

Received April 21, 2015; Accepted February 29, 2016

ABSTRACT

Improved geochronological methods and *in situ* isotopic (O, Hf) and trace element studies of zircon require a new physical model that explains its behaviour during crustal melting. We present results of numerical modeling of zircon dissolution in melts of variable composition, water content, temperature, and thermal history. The model is implemented in spherical coordinates with two moving boundaries (for the crystal and the surrounding melt cell outer edge) using simplified mineral phase relationships, and accounting for melt proportion histories as a function of melting and crystallization of major minerals. We explore in detail the dissolution of variably sized zircons and zircon growth inside rock cells of different size, held at different temperatures and undersaturations, and provide an equation for zircon survivability. Similar modeling is performed for other accessory minerals: apatite and monazite. We observe the critical role of rock cell size surrounding zircons in their survivability. Diffusive fill away from a dissolving 100 μm zircon into a large $>3\text{ mm}$ cell takes 10^2 – 10^4 years at 750–950°C, but zircon cores may survive infinitely in smaller than 1 mm cells. Heating followed by cooling for a similar amount of time leads to dissolution followed by nucleation and growth, but new zircon growth remains smaller than the original within the cell. The final zircon size is also investigated as a function of micro-zircons crystallizing on a front of major minerals, leading to shrinking cell sizes and bulldozing of Zr onto the growing zircon surface. We explore in detail the survivability and regrowth of zircon inside and outside dikes and sills of different sizes and temperatures, and in different rock compositions, on timescales of their conductive cooling and heating, respectively. For zircon-rich rocks, only the largest $>200\text{ m}$ igneous bodies are capable of complete dissolution–reprecipitation of typically sized zircons at significant distances from the intrusion. Smaller intrusions result in partial dissolution and rim overgrowth. Zircons captured near the contact of conductively cooling sills undergo more overgrowth than dissolution. In contrast, heat wave propagation from the sill will completely dissolve and reprecipitate zircons in Zr-poorer rocks many diameters of the sill away and often 10^3 – 10^4 years after the sill intrusion. A single thermal spike and melting episode is capable of generating the observed complexity of isotopically diverse and geochronologically zoned zircons. A MATLAB program is presented for users to apply in their specific situations.

Key words: zircon; monazite; diffusion; numerical modeling; crustal melting

INTRODUCTION

Zircon, as well as other accessory minerals such as rutile, apatite and monazite, is an important tool for geochronology, trace element and isotopic research (for reviews see Kempe *et al.*, 2000; Hanchar & Hoskin, 2003; Hoskin &

Schaltegger, 2003; Valley, 2003; Hermann & Rubatto, 2009). With the advent of new microanalytical isotopic techniques in the past decade, geologists can now easily and inexpensively unravel the geochronological and isotopic information stored inside these minerals. Refractory

accessory minerals are often inherited from earlier magmatic episodes, making them useful for tracking magma evolution and compositional history (Vazquez & Reid, 2002; Rubatto & Hermann, 2007; Claiborne *et al.*, 2010; Miller *et al.*, 2011; Schmitt *et al.*, 2011; Trail *et al.*, 2012; Drew *et al.*, 2013; Chamberlain *et al.*, 2014).

Zircons, in particular, can provide a time capsule to reveal the O and Hf isotopic evolution, and the trace element melting or differentiation histories of their host melts or rocks (e.g. Vervoort & Patchett, 1996; Valley, 2003; Wotzlaw *et al.*, 2012, 2014; Colón *et al.*, 2015). *In situ* U–Th–Pb ion microprobe dating of zircons has resulted in the recognition of both ‘short’ (<50 kyr) and ‘long’ residence times (>100 kyr) in the magmatic zircon record and in crystallizing intrusions and sub-volcanic magma bodies (Charlier & Zellmer, 2000; Reid *et al.*, 2011; Storm *et al.*, 2011). However, whereas U–Pb ion microprobe uncertainties for single analytical spots are adequate to recognize inherited xenocrystic cores (Fig. 1), the errors of these methods are sometimes too large (>10⁴–10⁵ years) to resolve crystallization histories for each zircon and make inferences about the duration of

zircon growth and the state in which zircons were stored (e.g. prolonged crystallization in a mushy magma, or punctuated episodes of growth and subsolidus storage). *In situ* dating of young zircons by U–Th disequilibrium methods provides better precision, but the best precisions are limited to young, <50 ka zircons (Charlier & Zellmer, 2000; Carley *et al.*, 2011; Storm *et al.*, 2011). The advent of the most precise method of zircon dating—chemical abrasion isotope dilution thermal ionization mass spectrometry (CA-ID-TIMS)—for whole or partial crystals allows the interrogation of zircon magmatic histories with 0.1% relative age precision (Schmitz & Schoene, 2007; Schaltegger *et al.*, 2009). These precisions translate into millennia (or even century) timescales for young magmatic bodies (e.g. < ±2000 years for 0.6–4 Ma tuffs; Rivera *et al.*, 2014; Wotzlaw *et al.*, 2014, 2015). By dating single zircons, we are now able to recognize and resolve processes of crystallization, hydrothermal alteration, and remelting of magma bodies within the overall timescale of magma solidification into rock. Such recognition is best for medium- to large-volume magma bodies that cool on

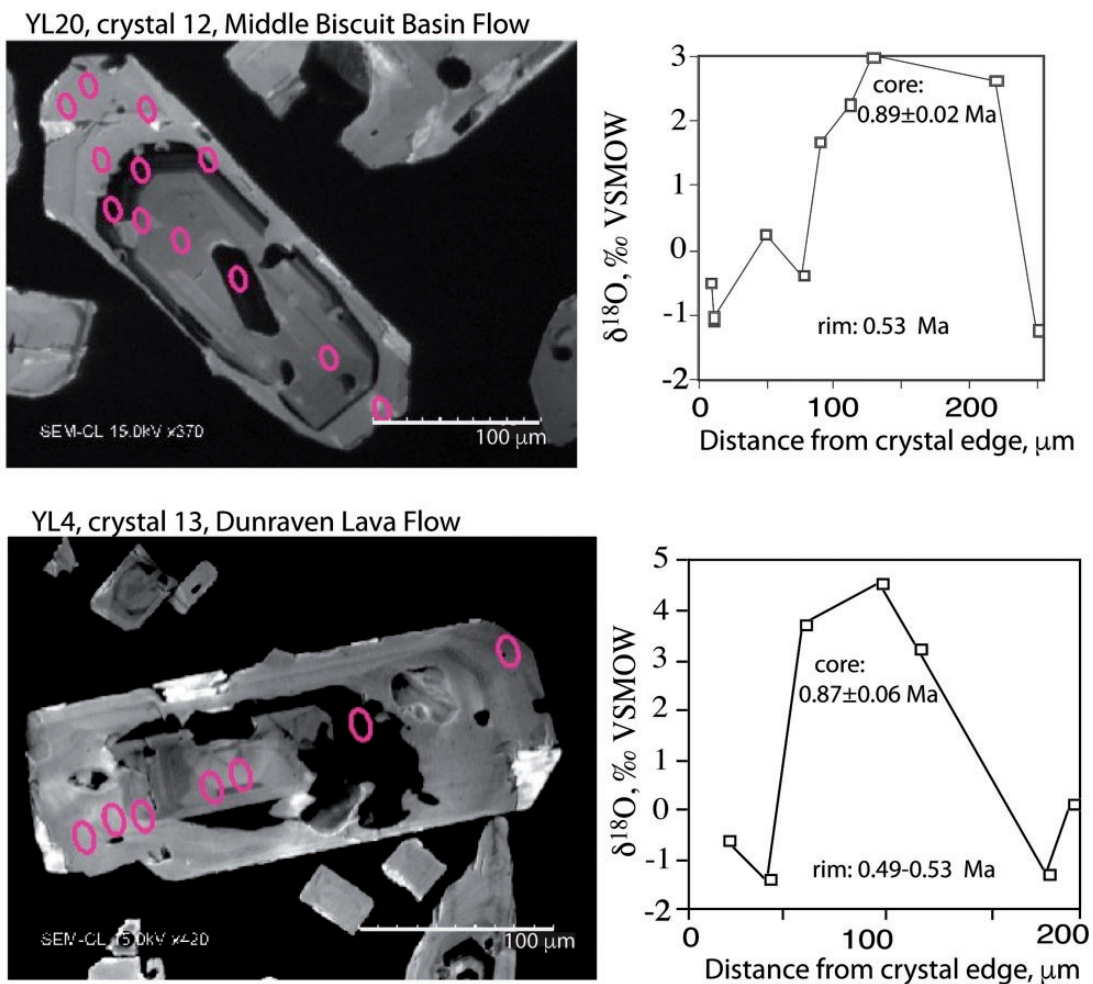


Fig. 1. Cathodoluminescence images, core and rim ages, dissolution boundaries and O isotopic zoning of zircons from Yellowstone [modified after Bindeman *et al.* (2008)]. Images demonstrate dissolution of surviving older, high- $\delta^{18}\text{O}$ cores into newly forming low- $\delta^{18}\text{O}$ (in d11O) O melt, followed by zircon regrowth that inherits these low- $\delta^{18}\text{O}$ signatures.

longer timescales. In particular, for large-volume 'hot and dry', near-liquidus rhyolites such as the Kilgore Tuff of the Heise volcanic field, and Lava Creek, Mesa Falls, and Huckleberry Ridge tuffs of Yellowstone (Bindeman *et al.*, 2008; Watts *et al.*, 2011), CA-ID-TIMS dating has now demonstrated that zircons can be dissolved and precipitated in less than 2–4 kyr (Wotzlaw *et al.*, 2014, 2015). However, very different records result from 'cold and wet', near-solidus rhyolites and dacites such as the Fish Canyon Tuff (zircon ages >150 ka, Bachmann *et al.*, 2002; Wotzlaw *et al.*, 2013).

Mineral diffusive and dissolutional processes provide a method for resolving shorter timescales than U–Th–Pb dating and are often used to predict months to decades timescales between magma recharge and eruption (Druitt *et al.*, 2012; Costa *et al.*, 2013; Carrichi *et al.*, 2014; Cooper & Kent, 2014). Recent discoveries of ubiquitous O and Hf isotope heterogeneities in zircons with nominally identical ID-TIMS ages (Bindeman & Simakin, 2014; Wotzlaw *et al.*, 2014, 2015; Colón *et al.*, 2015) suggest faster, tens to thousands of years processes of (1) melting of isotopically diverse protoliths above zircon saturation temperatures resetting U–Pb ages, followed by (2) new zircon crystallization from the immediate environment (melt cell), and then (3) segregation and mixing of these initial melts to make the (short-lived) magma body. The chaotic convective mixing of isotopically diverse magma batches results in diverse zircon populations in erupted rhyolites (Bea, 2010; Bindeman & Simakin, 2014).

These recent advances require a new model of zircon (and other refractory accessory minerals) survivability and recycling as a function of external and internal parameters. Much experimental work on accessory mineral solubility and diffusion has been done by E. B. Watson and T. M. Harrison and their collaborators over the past 30 years, as well as more recently by many other researchers (e.g. Rubatto & Hermann, 2007; Bernini *et al.*, 2013). Watson (1996) combined solubility and diffusion equations and presented a numerical treatment of zircon survivability that has remained an important milestone paper for the past 20 years. Here we advance the treatment in Watson's (1996) paper by providing an easy to use MATLAB-based computational platform for user-specific situations of zircon and other accessory mineral crystallization along T – $X(\text{H}_2\text{O})$ composition–time paths. This uses new experiments and parameterizations of zircon–melt saturation; it also uses a compilation of new diffusion coefficients parameterized to the temperature and water content of the melt, leading to about a two times shorter lifespan of zircons. We introduce optional M -factor dependence on temperature. The model uses a realistic situation of a finite melt reservoir (cell) around a zircon crystal and allows systematic study of the effect of the cell size on zircon dissolution and growth kinetics; zircon can be dissolved and then re-nucleate. Additionally, this study involves the influence of major mineral crystallization or dissolution on the finite melt cell size and on the Zr

concentrations at the far end of the cell. We also use a per cent melt versus temperature phase diagram that can be changed by the user, appropriate for both partially melted crustal rocks and near-liquidus rhyolites. Our study eliminates a small error in equation (12) of Watson (1996) in the conversion to spherical coordinates and in ignoring the $VC(r,t)$ term; this error, however, results in small differences from our computations (Supplementary Material Fig. A2; supplementary material is available for downloading at <http://www.petrology.oxfordjournals.org>), probably because of the typically small value of zircon growth rates, V . Our approach and computer code are easily convertible to other accessory phases, such as monazite and apatite, for which there are saturation and diffusion data.

METHODS: CONTROLLING PARAMETERS AND NUMERICAL MODEL

Description of parameters of the model and their physical meaning

Elementary cell and mass exchange within it

Figure 2 presents a conceptual view of zircon distribution in a rock and Fig. 3 outlines our model of a spherical zircon crystal surrounded by a melt cell with two moving boundaries. Given that melt cell sizes are much larger than the zircon size, zircons can be approximated as spheres (e.g. Watson, 1996) and the spherical model is the closest approximation to natural melting scenarios for accessory mineral within a certain cell size (Fig. 2). However, we also set up the initial model in linear and cylindrical coordinates. Figure A1 in the Supplementary Material compares dissolution outcomes, giving expectedly faster dissolution and growth for spherical coordinates.

Zircon growth and dissolution rates are limited by slow diffusion of zirconium (Zr) in and out of the crystal–melt interface (Fig. 3). Following Harrison &

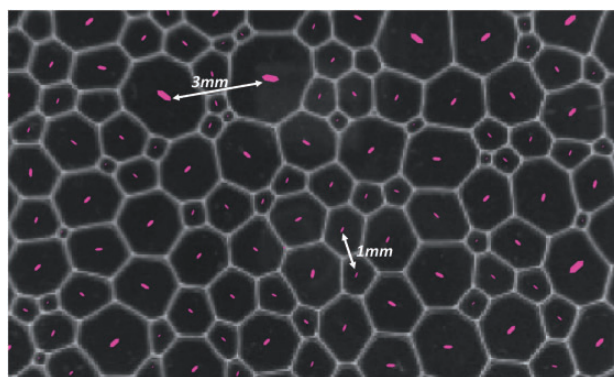


Fig. 2. Schematic model of measured zircon crystal size distribution and particle volume concentrations from sample YTT102 from the Youngest Toba Tuff (Table 1). The cell surrounding each zircon delineates a volume of diffusional sphere of influence that maintains identical Zr concentration at a cell's boundaries at equilibrium. Computed distances between large (230 μm , 3 mm cell) and median (75 μm , 1 mm cell) zircons are shown.

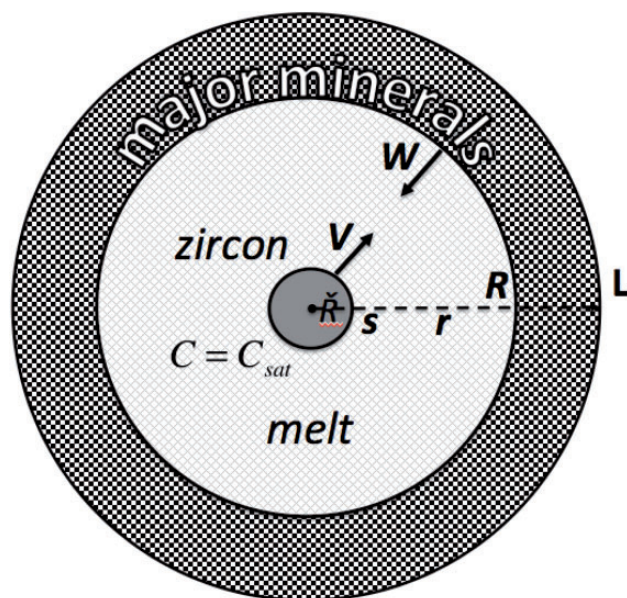


Fig. 3. Model set-up with zircon and melt cell volume and two independently moving boundaries with velocities V and W . The radius of the spherical diffusion cell is L . Saturation conditions are maintained at zircon of radius R at surface s ; Zr concentration C at the external melt boundary L is defined through the bulk partition coefficient of a major phase (with zircon microinclusions uniformly precipitated upon crystallization owing to bulldozing effects of a major Zr-free phase on contracting melt volume). The rate W of expansion or contraction of the melt volume is a function of a T - X phase diagram (Fig. 4c) and time.

Watson (1983), we assume local thermodynamic equilibrium between the crystal and the melt at the interface, $r = s$, where r is a radial coordinate, and s is the zircon surface. We note, however, that the outermost (~ 1 nm) surface of accessory minerals with a very high concentration of the constitutive element at their contact with the melt may have less trivial partition relations than major minerals (Rustad, 2015), but these effects are not implemented here. The boundary layer is the region adjacent to the interfaces, characterized by concentration gradients in the melt owing to dissolution or growth of the zircon. We assume that each zircon crystal is surrounded by a melt cell of a finite radius, L . The cell contains a zircon crystal in the center, surrounded by a melt layer $s < r < R$ and a layer of major element crystals $R \leq r \leq L$. The Zr concentration at the far end of the melt reservoir ($r = R$) should be primarily controlled by the diffusion of Zr coming from the dissolving zircon in the center of the cell. This concentration may also be affected by the crystallization of the major minerals (e.g. feldspar, quartz, biotite) owing to their very low concentrations of Zr and hence the build-up of Zr in front of their crystallization. It is possible to adjust partition coefficients to account for more compatible Zr behaviour; for example, owing to microzircon crystallization in the major phases' boundary layers (e.g. Bacon, 1989; see below). Although we set up the

model using zircon as an example, our numerical dissolution–crystallization experiments are also applicable for monazite and apatite.

Zircon sizes, number densities and distances between zircons and cell sizes

A very important parameter for any zircon dissolution and growth model is the model cell size and distance between single crystals. Thin section identification of minor abundance ($\ll 1$ vol. %) and small ($< 100 \mu\text{m}$) minerals does not provide adequate particle statistics to determine spacing. Instead, Bindeman (2003) performed acid dissolution of pumices from a series of well-known large and small eruption sequences and measured crystal size distribution (CSD) and quantitative particle number density per unit of magma volume for quartz and zircon. Examples given in Table 1 suggest that typically 28–300 single zircon crystals occupy each cm^3 of dense rock-equivalent, corresponding to an average distance between zircons of 3–0.6 mm prior to vesiculation, assuming equal spacing of particles. Using the example from the Youngest Toba Tuff (Fig. 2), which contains 96 zircons per cm^3 melt (Table 1), the measured average distance between twelve $> 150 \mu\text{m}$ zircons (with radius of $75 \mu\text{m}$), constituting half of the crystallized zircon volume, is 1.86 mm; and the single largest $230 \mu\text{m}$ zircon, constituting 10% of the total zircon volume, is 3 mm away from its equivalent in the next melt cell volume. These and other measurements in Table 1 provide an assessment of appropriate single zircon cell sizes to use in modeling. In particular, upon dissolution the largest zircons will survive the longest and be surrounded by the largest cell size. The cell size determines the length of diffusion away from a dissolving zircon–melt boundary.

Figure 2 presents a conceptual view of cells as diffusional spheres of influence for zircons of different sizes that would approximately satisfy measured zircon CSDs and estimated distances between particles of different sizes. We distinguish two geologically relevant situations with cell sizes. For an igneous or meta-igneous rock undergoing melting and crystallization, the distance between zircons of different size will be established by mutual interaction of the growing zircons upon the start of crystallization. As a result, a common collective CSD is maintained within each hand specimen-wide volume of rock (defining cells), containing 10^2 – 10^3 zircons (Table 1). For sedimentary and metasedimentary rocks that have been through chemical weathering and density water sorting, zircons and other accessory minerals may occur in layers, making distance between neighbouring zircons small in mafic layers and large in quartzo-feldspathic layers. Such a geometrical configuration will influence cell sizes upon heating, melting, and diffusional accessory mineral dissolution. Dissolution will be retarded in accessory mineral-rich layers, leading to their preservation, whereas in adjacent quartzo-feldspathic layers sparser

Table 1: Characterization of sizes, abundance, particle concentration of zircons from major tuffs and lavas, and distance between crystals

Tuff sample	Unit	Eruptive T $\Delta^{18}\text{O}(\text{Oz-Mt})$ (°C)	Crystal content (vol.%)	SiO_2 Zr (wt%)	Zr (ppm)	Conc. Zr (ppmv)	%Zr in zircon	n^* zircon cm^{-3}	Mean zircon (μm)	Median zircon (μm)	Max. zircon (μm)	Mean distance between zircon size (mm)†		Total zircons n
												200 μm	80 μm	
<i>Bishop (BT), Long Valley Caldera, CA, 750 km³, 0.76 Ma</i>														
LV-27	Early	714	9	78	89	12	13.5	28	94	89	210	2.58	0.86	500
LV-751	Late	761	15	76	118	16	13.6	37	88	88	240	2.26	0.74	367
LV-748	Late	817	13	73	140	17	12.1	67	99	99	260	1.24	0.74	352
LV-3	Late	763	27	73	138	27	19.6	98	78	72	240	1.68	0.56	614
LV-13	lava	801	15	72	200	51	25.5	345	35	26	190	4.68	0.78	544
<i>Lava Creek (LCT), Yellowstone Caldera, WY, 1000 km³, 0.64 Ma</i>														
LCT-3a, A	Early	809	11	78	187	14	7.5	37	37	95	250	1.42	0.74	304
YL-4	lava	882	9	76	393	70	17.8	325	84	80	280	2.96	1.08	430
<i>Huckleberry Ridge (HRT), Big Bend Caldera, WY, 2500 km³, 2.04 Ma</i>														
HRT-3a, A	Early	863	19	77	328	25	7.6	108	76	59	210	1.34	0.68	342
HRT-C, C	Late	897	21	75	445	33	7.4	114	95	88	230	1.68	0.56	343
<i>Mesa Falls (MFT), Island Park Caldera, ID, 300 km³, 1.3 Ma</i>														
MFT-1	Early	800	37	78	168	49	29.2	41	128	114	310	1.68	1.1	307
<i>Ammonia Tanks (AT), Timber Mountain Caldera, NV, 1000 km³, 11.45 Ma</i>														
TM-15	Early	809	14	76	215	22	10.2	67	84	76	300	3.16	0.52	637
TM-17	Late	842	20	73	293	16	5.5	47	77	71	300	2.76	0.64	508
TM-24	lava	776	7	76	135	8	5.9	125	42	37	185	4.56	0.86	160
<i>Youngest Toba Tuff, Toba Caldera, Indonesia, 2800 km³, 0.074 Ma</i>														
YTT-102	Early	752	27	75.6	107	28	26.2	96	75	69.0	230	1.86	0.56	404

* n is measured particle abundance per cm^3 of melt.

†Computed from measured zircon CSD and assuming equal spacing to maintain cell's constant Zr concentration. [See Bindeman (2003) for CSD and additional information for these samples.]

Table 2: Parameters and abbreviations used in this paper

r	radial coordinate in zircon cell (cm)
s	zircon surface of radius R , melt–zircon boundary
R	melt cell radius (mm)
L	rock (melt) cell (mm)
ξ	non-dimensional linear coordinate
V	growth or dissolution rate of zircon (cm s^{-1})
W	growth or dissolution of the major phases at the outer cell boundary
C_m	concentration of zirconium in the melt
C_z	(= 490,000 ppm) Zr concentration in zircon
C_x	concentration of Zr in a major phase
C_{bulk}	bulk Zr concentration in a rock or cell (zircon plus melt)
K_{Zr}	bulk Zr partition coefficient between major phase and melt, $C_{\text{Zr}}^{\text{major}}/C_{\text{Zr}}^{\text{melt}}$
C_{sat}	T and M -factor dependent saturation concentration (Watson & Harrison, 1983; Boehnke <i>et al.</i> , 2013)
ΔU	Zr undersaturation relative to C_{sat} (ppm of Zr)
M	M factor, = $(\text{Na} + \text{K} + 2\text{Ca})/(\text{Al} \times \text{Si})$, where elements are given in molar proportion inside 1 mol of silicate melt
D	diffusion coefficient of Zr in melt, dependent on temperature T and $X_{\text{H}_2\text{O}}$ ($\text{m}^2 \text{s}^{-1}$)
$X_{\text{H}_2\text{O}}$	water wt % fraction in melt
T	temperature ($^{\circ}\text{C}$ or K)
T_{eutectic}	eutectic temperature ($^{\circ}\text{C}$)
T_d	temperature of the dike or sill
T_c	temperature of the country rocks
X	composition (% crystal)
k	thermal diffusivity in rocks and magmas ($0.6 \times 10^{-6} \text{ m}^2 \text{ s}^{-1}$)
h	dike or sill thickness (m)
x	linear coordinate from dike or sill center outward (m)

accessory phases will undergo enhanced dissolution upon heating (see below). Furthermore, zircons can become occluded by other Zr-free phases. Bea & Montero (2013) numerically described the conditions for zircon survival when shielded by other phases. Microscopic inclusions of zircons are present in many biotites, amphiboles, and rarely feldspars. Bacon (1989) described saturation with accessory minerals on the boundary of crystallizing feldspars, a topic that we address below by numerical modeling.

In our model, for a given size of zircon, cell size can be specified either independently or by the bulk Zr concentration in a rock, which is a function of zircon mass and ambient melt Zr concentration. In both melting and crystallization, the zircon boundary layer will maintain C_{sat} concentration, and diffusion will strive to attain equilibrium across the cell. There is no flux between adjacent cells because it is assumed that the neighbouring cells with zircons of different size (Fig. 2) contribute Zr via diffusion uniformly in N adjacent cells around the cell of interest. When selecting zircon size, cell size, and temperature, the model allows for selection of zircon under- or over-saturation conditions via the parameter ΔU (see below). Such an initial condition may correspond to instantaneous temperature overstepping (thus different C_{sat}), or zircon appearance in a melt of different composition, and thus C_{sat} , owing to rapid mixing of magmas with different Zr concentrations, for example.

Zirconium diffusion in melt

Dissolution of minerals in high-viscosity, low-diffusivity silicate melts is almost always controlled by slow diffusion through the melt of their constituent elements (Zhang *et al.*, 1989; Zhang *et al.*, 2010). In the case of zircon,

apatite, and monazite, the diffusion coefficients of their constituent 3+, 4+ and 5+ elements have $D = 10^{-12}$ – $10^{-15} \text{ cm}^2 \text{ s}^{-1}$ at relevant magmatic temperatures (700–1200 $^{\circ}\text{C}$; Harrison & Watson, 1983; Zhang *et al.*, 2010, and references therein), the lowest compared with major oxides (Baker, 1991; Acosta-Vigil *et al.*, 2006). The diffusion coefficient of zirconium, D , is a function of temperature, T , and water content, $X_{\text{H}_2\text{O}}$ (Harrison & Watson, 1983; see Table 2 for parameters and units). Heat diffusion and diffusion of water are orders of magnitude faster than the diffusion of Zr (Zhang *et al.*, 2010); thus, we can assume instantaneous equilibration of the temperature and the water concentration within the cell and consider these parameters as external.

Water decreases activation energies and increases diffusion coefficients by 2–3 orders of magnitude between 950 and 650 $^{\circ}\text{C}$ (Watson & Harrison, 1983; Harrison & Watson, 1984; Rapp & Watson, 1986; Xu & Zhang, 2009; Zhang, 2012). This effect is likely through making diffusion clusters and increasing the amount of non-bridging oxygen or OH^- atoms and molecules available for charge compensation during diffusive jumps of highly charged cations. Harrison & Watson (1983, 1984) and Zhang *et al.* (2010) noted that the addition of the first 1–2 wt % of water produces the most dramatic effect on the acceleration of diffusion, by several orders of magnitude, but the effect of further water addition from 3–4 to 6 wt % increases D by less than a factor of five. We compiled published diffusion coefficients for Zr at different temperatures and water contents as given by Zhang *et al.* (2010), with most data from Watson's and Harrison's experiments. These experimentally determined relationships are parameterized in our model as

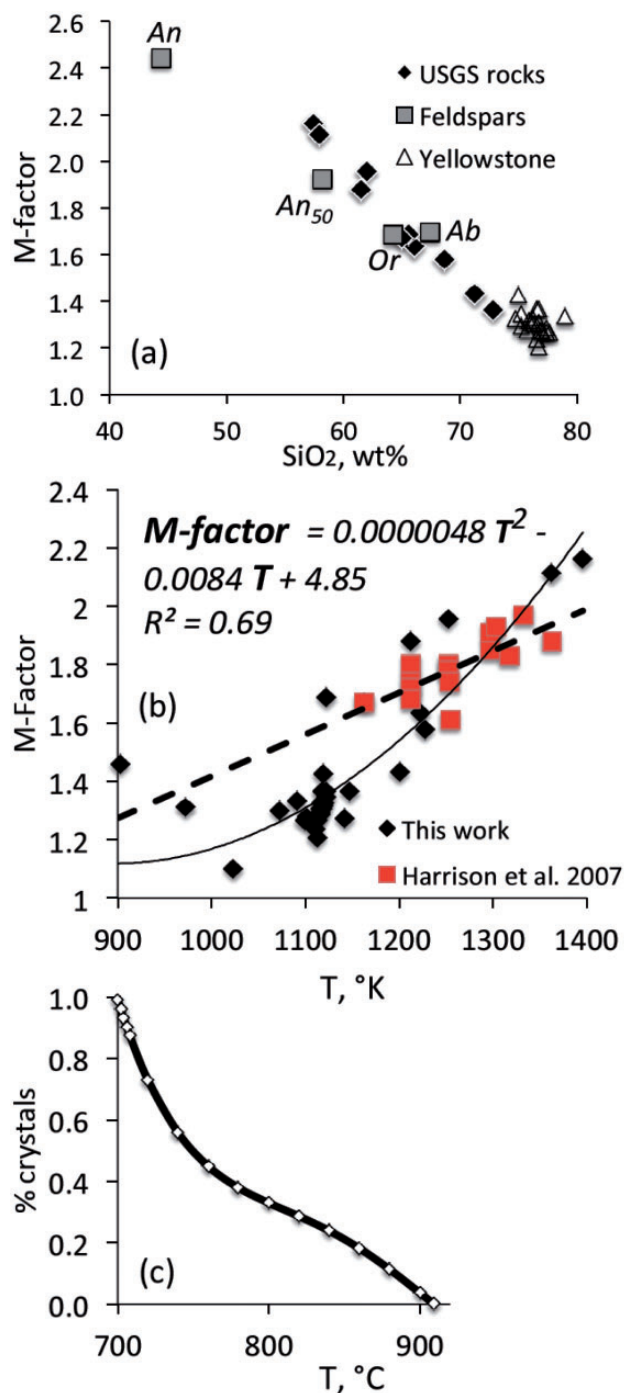


Fig. 4. *M*-factor dependences and phase diagram. *M*-factor variations as a function of SiO₂ for standard USGS rock compositions (from andesite to rhyolite), Yellowstone magmas and feldspar end-members. It should be noted that quartz-free, feldspar-rich compositions and lower silica melts have higher *M* factors. *M*-factor dependence on temperature for the liquidus compositions of melts shown in (a) is computed at 3 wt % water and the computed liquidus using MELTS. (See Supplementary Material for compositions and temperatures used.) Phase diagram (solidus–liquidus relations) used in this work is based on the crystallization experiments of starting composition 102 at 2 kbar (Piwinski, 1968). The best-fit line is given as % melt fraction = $1.13656 \times 10^{-9} T^4 - 3.8926 \times 10^{-6} T^3 + 4.9848 \times 10^{-3} T^2 - 2.832 T + 602.99$, where *T* is in °C.

$$\ln(D) = -\frac{11.4X_{\text{H}_2\text{O}} + 3 \cdot 13}{0.84X_{\text{H}_2\text{O}} + 1} - \frac{21.4X_{\text{H}_2\text{O}} + 47}{1.06X_{\text{H}_2\text{O}} + 1} \cdot \frac{1000}{T}. \quad (1)$$

This approximation does not take into account the influence of melt *F* and *Cl* content on Zr diffusion, which have strongly different activation energies for diffusion (Baker & Watson, 1988).

Zircon saturation C_{sat} and compositional *M* factor

A series of dissolution–crystallization experiments for zircon in melts with a range of compositions, water contents and temperatures were conducted by Harrison & Watson (1983), Watson & Harrison (1983), Rubatto & Hermann (2007), Hermann & Rubatto (2009) and Boehnke *et al.* (2013) and calibrated for C_{sat} dependence on *T* and composition. The compositional factor that affects zircon solubility is defined as $M = (\text{Na} + \text{K} + 2\text{Ca}) / (\text{Al} \times \text{Si})$, where elements are given in molar proportions. Increasing alkali content and melt peralkalinity increases zirconium solubility and thus larger *M* factors require higher Zr concentrations to cause zircon saturation. Boehnke *et al.* (2013) presented an updated calibration of the Watson & Harrison (1983) model, where C_{sat} is a function of *T* and *M*:

$$C_{\text{sat}} = 490000 / \exp \left[\frac{10108}{T} + 1.16(M - 1) - 1.48 \right]. \quad (2)$$

M factors may decrease with igneous differentiation. We performed MELTS and RhyoliteMELTS (Ghiorso & Sack, 1995; Gualda *et al.*, 2012) crystallization experiments on a series of USGS standard rock compositions to model *M*-factor dependence on *T* and composition (Fig. 4). We note that because pure feldspar endmembers have large *M* factors, and quartz has an *M* factor = 0, melting of a silicic assemblage will lead to the progressive increase in partial melt *M* factor upon dissolution of quartz, then decreasing proportions of Ab and Or in feldspars, which move towards more An-rich compositions. The function of *M*-factor dependence on temperature (K) that was used in this work (Fig. 4b) is

$$M = 4.8 \times 10^{-6} T^2 - 8.4 \times 10^{-3} T + 4.84. \quad (3)$$

Our results are comparable with earlier statements by Watson & Harrison (1983), Miller *et al.* (2003) and Boehnke *et al.* (2013) that multiply saturated silicic melts have *M* factors within a narrow range of 1.3–1.8. A second-order polynomial approximation better reflects the expected shallowing of *M* factors with decreasing temperature as the granitic eutectic (and thus constant composition) is approached than a linear extrapolation of the higher temperature experimental data [e.g. $M = 0.5 + 0.0013 T(^{\circ}\text{C})$ used by Harrison *et al.* (2007)]. It is also possible to keep the *M* factor constant within a melting–crystallization regime within our program.

Temperature–per cent melt relations and crystallization of major minerals

Upon melt cooling or heating, crystallization or melting–dissolution of zircon from its defined cell will also be accompanied by crystallization or melting of major silicate phases such as feldspars, quartz, and pyroxenes (Fig. 3). The general topology of the granitic eutectic includes increases in $x\%$ (crystal content) at small variations in T . Increasing pressure and water content results in the eutectic temperature decreasing to a minimum of $\sim 630^\circ\text{C}$ at ~ 10 kbar (Clemens & Vielzeuf, 1987); shallow 1–2 kbar silicic systems such as the Fish Canyon or Bishop Tuffs have eutectic temperatures of 710 – 750°C (Hildreth, 1979; Bachmann *et al.*, 2002). Low-temperature magmas such as these are almost always water-saturated with at least 4 wt % and commonly up to 6 wt % water (Wallace *et al.*, 1999). Liquidus temperatures are more strongly affected by the initial water content than the solidus, which is likely to be always water-saturated (Holtz, 1992). Hot and dry Yellowstone and Snake River Plain rhyolites may contain only 1–2 wt % water at the liquidus (e.g. Almeev *et al.*, 2012) and thus have high temperatures of 850 – 950°C (Loewen & Bindeman, 2016), but even these will reach 4–5 wt % water and thus an $\sim 750^\circ\text{C}$ low-pressure eutectic and solidus at higher degrees of crystallization. It is thus important (but not critical as our modeling shows) to set up the preferred T –per cent melt function for a cell that is undergoing zircon dissolution. Anatectic melts formed by the dehydration of amphibolites and gneisses can be user-defined, based on the most realistic situations.

As none of the major rock-forming minerals take up Zr, the bulk Zr partition coefficient between these minerals and melt is close to zero ($\sim 10^{-1}$ – 10^{-4} ; see <http://earthref.org/KDD> for partition coefficients); pyroxene, amphiboles and garnets have slightly higher K_{Zr} in the 0.1–0.6 range, but they rarely crystallize without feldspars ($K_{Zr} < 0.01$), leading to bulk $K_{Zr} \ll 0.1$. The effect of the crystallization–melting of major minerals on zircon growth–dissolution is significant, especially at higher crystallinity where major phase growth will affect bulk melt Zr concentration in the vicinity of zircon crystals. The compositional effect of major phase crystallization is implemented at the independent boundary of zircon cells (Fig. 3). Crystallization leads to movement of the melt–major phase interface at a rate W , which is determined by the temperature–per cent melt relation function, and the partition coefficient for Zr for major phases, K_{Zr} , defined in the program or set up by the user. Microzircon inclusions may nucleate on the front of their crystallization.

Zircon nucleation

Upon cooling of a melt cell volume, zircon is allowed to nucleate in an area exceeding C_{sat} concentration by oversaturation, $-\Delta U$. The center of the cell normally contains undissolved zircon (or shortly thereafter, a trace memory of higher Zr concentration left after zircon

dissolution), favoring nucleation to proceed there. Nucleation is implemented in the model by setting up a small oversaturation $-\Delta U$ of 0.5–5 ppm, defined by the user. Nucleation of zircon owing to oversaturation near an advancing external cell boundary of growing major phases is not explicitly realized owing to the one-dimensional, spherical coordinate set up of our model, but it is realized through microzircon nucleation and its effect on the bulk phase K_{Zr} value (Fig. 3; see below).

Equations and boundary conditions

Transport of Zr in the melt cell is governed by the standard diffusion equation, which in a spherical case can be written as

$$\frac{\partial C}{\partial t} = \frac{D(T, X_{\text{H}_2\text{O}})}{r^2} \frac{\partial}{\partial r} \left(r^2 \frac{\partial C}{\partial r} \right). \quad (4)$$

Here C is the concentration, measured in ppm, r is the radius measured from the centre of the zircon crystal, and t is the time (Table 2). Equation (4) is solved only inside the melt part of the cell $s < r < R$, because diffusion of Zr in the major crystal phases is very slow in comparison with the diffusion in the melt.

Boundary conditions at the crystal–melt interface ($r = s$) indicate local thermodynamic equilibrium and mass conservation of zirconium:

$$r = s : -D \frac{\partial C}{\partial r} \Big|_{r=s} = J = V[C_m - C_z]; C_m = C_{\text{sat}}(T). \quad (5)$$

Here V is the growth rate of zircon, C_m is the concentration of Zr in the melt, and $C_z = 490,000$ ppm is the Zr concentration in zircon. The saturation concentration C_{sat} of Zr mainly depends on temperature and melt composition, which are governed by the equations of Watson & Harrison (1983) and Boehnke *et al.* (2013), which are integrated into the model. On the outer melt boundary ($r = R$; Fig. 3) mass partitioning of Zr between major minerals and the melt is specified by

$$r = R : -D \frac{\partial C}{\partial r} \Big|_{r=R} = J = W[C_m - C_X]; C_X = K C_m. \quad (6)$$

Here W is the velocity of the outer boundary, C_X is the concentration of zirconium in major minerals, and K is the Zr distribution coefficient, $C_{Zr}^{\text{major}}/C_{Zr}^{\text{melt}}$. Discussion of particular values of the parameters in equations (1)–(3) is presented below.

To solve equation (4) with boundary conditions (2) and (3) we first make a coordinate transformation to a moving domain:

$$\xi = \frac{r-s}{R-s}; \quad \xi(r=s) = 0; \quad \xi(r=R) = 1. \quad (7)$$

This transformation allows equation (4) to be solved in a fixed coordinate frame. After application of equation (7), equation (4) becomes

$$\frac{\partial C}{\partial t} + \frac{V(\xi-1) - W\xi}{R-s} \frac{\partial C}{\partial \xi} = \frac{D(T, X_{\text{H}_2\text{O}})}{(R-s)^2 r(\xi)^2} \frac{\partial}{\partial \xi} \left[r(\xi)^2 \frac{\partial C}{\partial \xi} \right]. \quad (8)$$

Boundary conditions do not change their functional form except for the calculation of the fluxes:

$$\xi = 0 : -\frac{D}{R-s} \frac{\partial C}{\partial \xi} \Big|_{\xi=0} = V[C_m - C_z]; C_m = C_{\text{sat}}(T). \quad (9)$$

$$\xi = 1 : -\frac{D}{R-s} \frac{\partial C}{\partial \xi} \Big|_{\xi=1} = W[C_m - C_x]; C_x = KC_m.$$

The system [equations (8) and (9)] is discretized using a finite volume approximation assuming a fully implicit scheme. The resulting 3-diagonal matrix linear equation is solved by the Thomas method (Conte & deBoor, 1972), which is unconditionally stable. This allows the model to make no restrictions on the time step based on the CFL (Courant–Friedrichs–Lewy) condition (Courant *et al.*, 1928). Mesh independence of the results was achieved by comparison of solutions with finer and coarser meshes and a simultaneous decrease in the time step. The programming was realized in MATLAB and the code is available in the [Supplementary Material](#).

RESULTS

Below, we first explore the dependences of different parameters on each other, using numerical experiments of zircon dissolution at different temperatures and degrees of undersaturation in cells of different size, followed by dissolution and crystallization at different rates of heating and cooling. Second, we consider zircon dissolution and crystallization over geologically realistic timescales and thermal histories, by integrating our model with a model of conductive cooling and heating by intrusion of magma bodies (dikes and sills) into the crust.

Dissolution at constant temperatures but different cell size and ΔU

At any T , zircons may be kept undersaturated ($\Delta U > 0$), oversaturated ($\Delta U < 0$) or in equilibrium ($\Delta U = 0$) with their surrounding melt cells. From a geological point of view, rapid or instantaneous changes in saturation can be achieved by: (1) zircons being captured into a different (under- or oversaturated, hotter or colder) melt in the course of magma mixing or rapid disaggregation of solid fallen roof material (e.g. Bacon & Lowenstern, 2005; Beard *et al.*, 2005; Acosta-Vigil *et al.*, 2010; Simakin & Bindeman, 2012) leading to rapid zircon contact with melts; or (2) rapid (overstepping) temperature increases or decreases leading to zircon under- or over-saturation. Contact metamorphism, roof melting, stoping, and rapid target rock melting upon meteorite impact (e.g. Cavosie *et al.*, 2010) are examples of likely scenarios. Typically more sluggish temperature changes during deep to mid-crustal anatexis in metamorphic rocks and migmatites, and in subduction zones, may mean that temperature will control the saturation conditions of zircon and other minerals. However, fluctuation of the amounts and compositions of fluids in migmatites (Rubatto *et al.*, 2006) and in subduction zones (e.g. Hermann & Rubatto,

2009), coupled with fracture dynamics, may produce punctuating regimes of zircon under- or over-saturation within its own cell upon melting. Bulk compositional control matters too: for mafic rocks containing detrital zircon such as amphibolites and metagreywackes, melting will result in zircon-undersaturated melts, whereas for zircon-rich layers in a gneiss melting will result in Zr oversaturation.

Effect of cell size

Figure 5 shows the amount of time required for zircon dissolution at different levels of undersaturation inside a melt cell volume of fixed size. By varying the cell size (Fig. 6) at a given Zr undersaturation and constant temperature we investigated the kinetics of zircon dissolution—how long does it take for zircon of a given size to either (1) dissolve completely within a melt cell (Fig. 5a) or alternatively (2) dissolve to a smaller size and reach Zr saturation within it (Fig. 5b). As illustrated in Fig. 5, the outcome depends simply on the total bulk

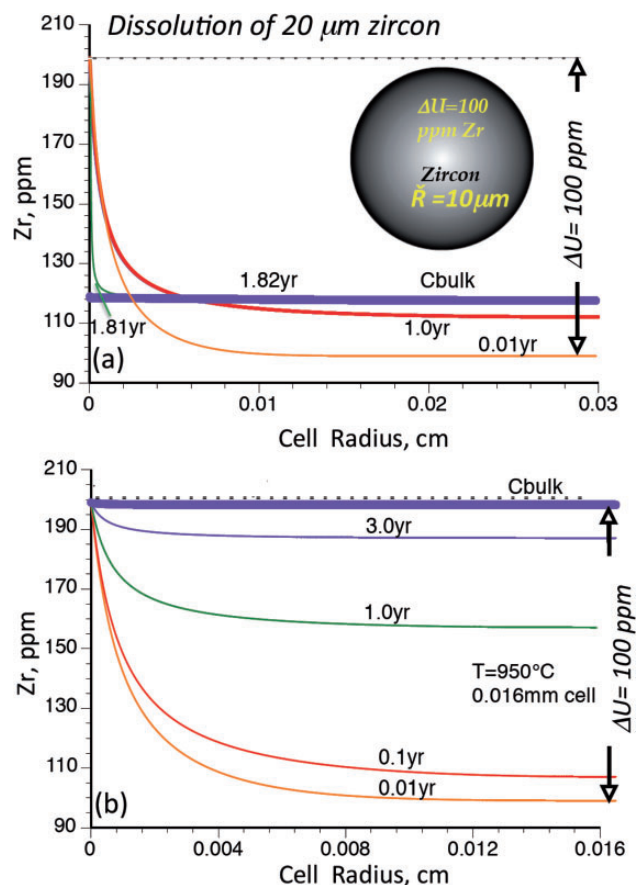


Fig. 5. Dissolution kinetics of a small (20 μm –10 μm radius) zircon into melt with $\Delta U = 100$ ppm of initial Zr undersaturation at 950°C in different cell volumes (cell radius – distance). For the 0.3 mm cell, zircon dissolves completely to C_{bulk} value of 119 ppm in 1.82 years. The steepening of the diffusion profile just before complete dissolution at 1.81 years should be noted. For the 0.16 mm cell, 5 μm zircon core survives and provides enough Zr to fill the melt cell around it with $C = C_{\text{sat}}$ of 199 ppm.

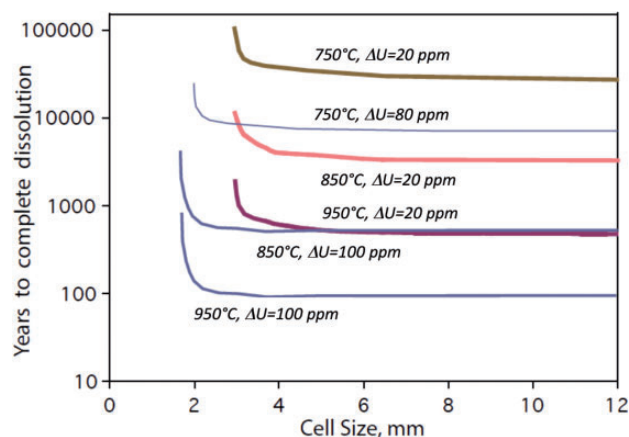


Fig. 6. Zircon dissolution timeframes for crystals of 100 μm radius, as a function of melt volume cell size, temperature, and degree of original melt Zr undersaturation, ΔU . It should be noted that cells greater than 2–3 mm are ‘infinite’ leading to nearly permanent sharp dissolution gradients and comparable dissolution times. At 950°C these times are 100–400 years at 20 and 100 ppm undersaturation, and at 750°C the times are 30–50 kyr, owing to both slower diffusion of Zr in the melt and lower zircon solubility, diminishing the overall diffusive flux.

concentration of Zr within a cell (zircon + melt) and C_{sat} ; if $C_{\text{bulk}} > C_{\text{sat}}$ zircon will survive, alternatively it will be dissolved. Zr undersaturation, ΔU , has an equivalence in temperature of 8°C per 10 ppm Zr using the saturation formulation of Boehnke *et al.* (2013). Such outcomes are easy to understand by thinking of dissolution of a single NaCl crystal in undersaturated water solutions of various volumes (cell size), kept at different temperatures. However, the difference between the NaCl–water solution analogy and zircon–melt is that zircon contains 490,000 ppm Zr whereas much lower Zr concentrations of between 10 and 10³ ppm Zr are required for zircon saturation in silicate melts (e.g. Harrison & Watson, 1983); thus tiny amounts of zircon dissolution will saturate the melt. Additionally, unlike the almost instantaneous saturation of the water solution with dissolving NaCl, the filling of the cell with Zr and the resulting achievement of equilibrium zircon size takes a long diffusional time. The NaCl analogy may also be thought of for a major mineral, such as plagioclase–melt.

Models at 950°C and M factor = 1.8 and different ΔU (Fig. 6) demonstrate the role of cell size in determining zircon survivability. Dissolving zircon fills small cells with Zr more quickly, decreasing diffusion gradients and increasing the dissolution time. Increasing cell size to >3–4 mm rapidly accelerates dissolution rates and reduces dissolution time. At 20 ppm undersaturation and large cell sizes, it will take 400 years to dissolve a 100 μm radius zircon, whereas 1600 years is required to dissolve zircon inside a 3 mm cell size to reach $C_{\text{bulk}} = C_{\text{sat}}$. Further, dissolution time does not significantly decrease with an increase in cell sizes past 3–4 mm, providing a minimum time estimate for zircon dissolution at a given undersaturation.

Effects of changes in ΔU and temperature

Not surprisingly, as temperature affects both C_{sat} and diffusion coefficients (Harrison & Watson, 1984), the survivability of zircon is strongly dependent on the temperature at a given ΔU and cell size (Fig. 6). A temperature increase of 100°C shortens the total dissolution time of a large 100 μm zircon in a melt with $\Delta U = 20$ ppm by a factor of 10.

An increase in undersaturation ΔU from 20 to 100 ppm decreases the minimum dissolution time by a factor of ~ 4.5 for zircon of identical size (Fig. 6). For experiments at 750°C and small ΔU of 20 ppm, minimum zircon dissolution times in large cells are measured at 30, 50, and 100 kyr in smaller cells. For 80 ppm maximal possible undersaturation (so $C_{\text{sat}} - \Delta U = 0$) dissolution times are 7–10 kyr. At an intermediate temperature of 850°C, dissolution at $\Delta U = 20$ and 100 ppm in 5 mm cells takes 3.5 kyr and 0.55 kyr respectively. These dissolution experiments demonstrate that only large $\Delta U > 50$ ppm undersaturation plays a significant role in accelerating zircon dissolution. Because of the rather steep increase in C_{sat} with T (e.g. 8°C per 10 ppm, Boehnke *et al.*, 2013), undersaturation increases the concentrational gradients near the dissolving zircon boundary and tiny amounts of zircon dissolution rapidly decrease the effect of the original undersaturation.

Dissolution and growth rates

Figure 7 considers the dissolution rates, V , of different sized zircons inside a large 5 mm cell, which is almost infinite relative to the zircon crystal size. The dissolution rate at first is nearly constant and then slowly increases after dissolution of the outer $\sim 20\%$ of the original zircon radius. The dissolution of the final 20% of the original radius (or remaining 1% of the zircon volume) proceeds with accelerating rate. This relationship is a simple outcome of radial diffusion in spherical coordinates, directly applicable to natural conditions. The boundary condition [equation (5)] along the dissolving zircon boundary requires an accelerating V to keep up with the required supply of Zr from the smaller and smaller surface area of a shrinking crystal. The same effect is illustrated in Fig. 5a, where the diffusion gradient (and thus rate of dissolution) is greater for smaller zircons. The 10 μm zircons start dissolution at about 10 times faster rates than 100 μm zircons. The rate increases twice for the dissolution for the last 2 μm (see steep profile at 1.81 years in Fig. 5a). This rather simple result has important implications for zircon survivability; small zircons will dissolve disproportionately faster at any change in T leading to undersaturation, explaining the common occurrence of concave-up zircon crystal size distributions in igneous rocks (Bindeman, 2003; Simakin & Bindeman, 2008). Modeling expectedly shows that the reverse is also true; upon nucleation, zircon growth rate is also faster for smaller crystals (Fig. 7b).

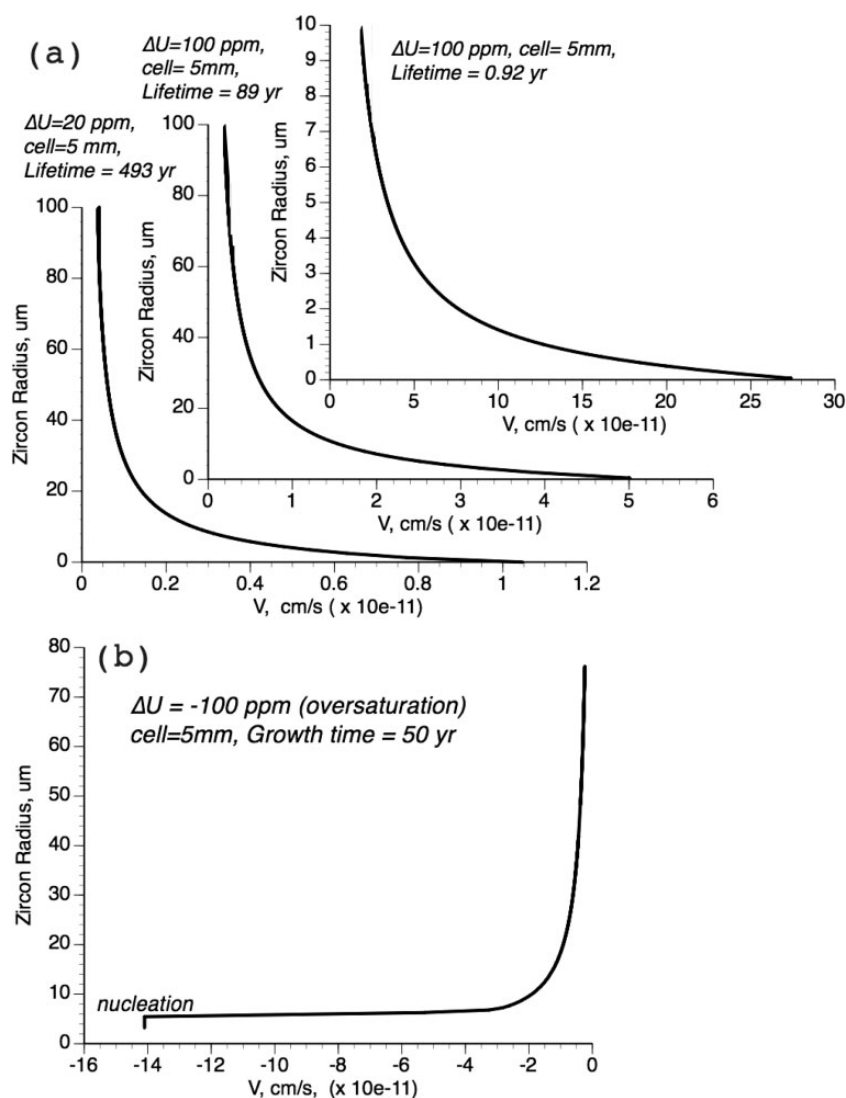


Fig. 7. (a) Dissolution rates of 10 and 100 μm zircons (upper graph) as a function of remaining zircon radius within 5 mm cell volume at 950°C for 20 and 100 ppm Zr undersaturation (ΔU). The increase of dissolution rate with shrinking crystal size for each case should be noted; this is explained by the increasing surface/volume ratio. For a small (10 μm) zircon, diffusion is essentially an open boundary condition, whereas a 100 μm zircon with 20 ppm of undersaturation leads to the longest dissolution time as back-diffusion from the boundary of the cell slows the dissolution rate. (b) Growth rate of an originally 5 μm radius zircon at 100 ppm oversaturation within a 5 mm cell volume, showing a similar growth rate size dependence.

Approximation of dissolution and growth rates

The above estimates (Figs 5–7) should provide the reader with expected timescales of zircon dissolution–crystallization in realistic ranges of T and ΔU . To quantify this, we performed 100 growth and dissolution runs at different constant temperatures and degrees of undersaturation for zircons of variable size. We used cells greater than 4 mm (Fig. 6) in which there is little dependence of zircon growth or dissolution rate on cell size. The total Zr concentration in the rock in these runs varied from 50 to 500 ppm.

The approximation fit using DataFit software leads to the following expressions for rates, V , and zircon radius, \bar{R} , tested for zircon radii between 30 and 90 μm and T from 650 to 950°C:

$$V\bar{R}^n(10^{15}) = X_2 \exp(-0.034 + 13.4X_1 - 2.90X_1^2) \quad (10)$$

$$n = 0.991 - 0.0247X_1 - 0.116X_2 - 0.0071X_1^2 + 0.0603X_2^2 - 0.17X_1X_2 \quad (11)$$

where $X_1 = [T(^{\circ}\text{C}) - 650]/300$ and $X_2 = \Delta U/C_{\text{sat}}$, where C_{sat} is a $f(T)$ (values of these variables change from zero to unity). These equations can be used to estimate the survivability of zircons of different sizes in user-specific static situations. They have been compared with equation (17) of Watson (1996) and predict 20–40 times faster dissolution of zircon (Supplementary Data Fig. A2).

Linear temperature increase from solidus to liquidus at different rates

In the previous section our models examined the case of instantaneous achievement of zircon under- or oversaturation (parameter $\pm \Delta U$). We next explore how different rates of temperature increase and decrease will

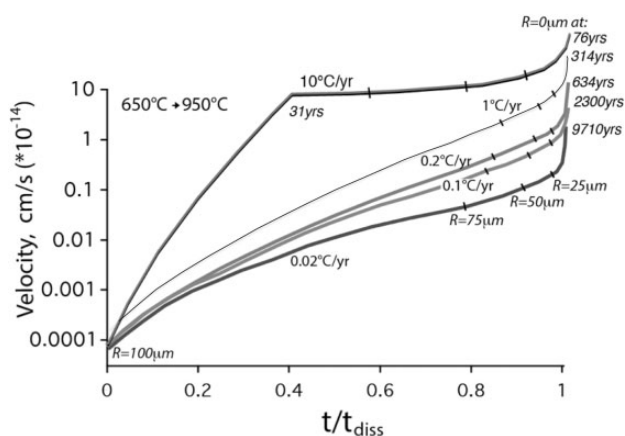


Fig. 8. Zircon dissolution owing to linear rock heating from the solidus at 650°C to the liquidus at 950°C at different rates of temperature increase ranging from 0.02 to 10°C a⁻¹, leading to complete zircon dissolution at indicated years. Velocity (in cm s⁻¹) refers to the moving dissolving zircon–melt boundary; t/t_{diss} is time normalized to the total dissolution time given in years next to each line. Original zircon radius $R = 100\ \mu\text{m}$; remaining zircon radius is shown by tick marks; bulk cell Zr concentration (zircon + melt) is 220 ppm; computed original cell size is $L = 1.72\ \text{mm}$ and expands to 2.2 mm upon major minerals melting; original $\Delta U = 0$. It should be noted that at rates higher than 5°C a⁻¹, the Zr concentration in the cell cannot keep up with the rate of T increase so that the zircon dissolution rate and time to complete dissolution is ~ 50 years. This time is comparable with that for dissolution in a melt at a constant T of 950°C (e.g. Fig. 7), with Zr undersaturation of 185 ppm [C_{sat} difference between 650 and 950°C, in accordance with equation (2) in text].

affect zircon dissolution–crystallization inside a cell volume of the same size, while keeping $\Delta U = 0$. As the diffusion of Zr in the melt is highest at the higher T , we explore the relation between the rate of temperature increase and the slow Zr diffusion reaction to ‘overstepping’ temperature, before diffusion from the zircon boundary can adjust.

Different rates of linear T increase

Linear rock heating from the solidus at 650°C to the liquidus at 950°C was performed at different rates ranging from 0.02°C a⁻¹ to 10°C a⁻¹, all resulting in complete zircon dissolution (Fig. 8). We observe that dissolution at $dT/dt < 1^\circ\text{C a}^{-1}$ is primarily controlled by the rate of temperature increase (the rate the C_{sat} at the higher temperature is crossed). At rates higher than 5°C a⁻¹, it is the slow diffusional cell fill with Zr that determines (slows down) the dissolution rate. At dT/dt between 1 and 5°C, these rates are influenced by both the rate of T increase and slow Zr diffusion. Thus, at rates higher than 5°C a⁻¹, dissolution and diffusion away from the dissolving boundary cannot keep up with the rapid rate of T increase owing to the slow diffusion of Zr in the cell. As a result, zircon dissolution rates and minimum times to complete dissolution (which are ~ 50 years in this case) are comparable with dissolution at a terminal and constant 950°C (Fig. 6). Very rapid temperature increases can be viewed as putting the original zircon in a

pre-set undersaturation equivalent to $\Delta U = 185\ \text{ppm}$ (C_{sat} difference between 650 and 950°C).

Realistic heating and cooling rates owing to conductive heat fluxes from cooling igneous bodies are modeled below and are shown in Supplementary Material Fig. A3. Heat is transferred via conduction and rarely exceeds 1°C a⁻¹ and then only for a short period of time, next to the contact with a sill. Translated to natural scenarios, this is applicable to contact metamorphism or melting caused by the intrusion. Higher rates of conductive heating are thus rarely realized (e.g. Huppert & Sparks, 1988). Instantaneous heating is equivalent to a small piece of rock or zircon captured and submerged in a magma of different temperature and ΔU , or to rapid magma mixing, similar to what is modeled in Fig. 5. Much lower rates of heating or cooling are realized in far fields of cooling dikes and sills and in regional metamorphism or anatexis ($< 0.02^\circ\text{C a}^{-1}$, Fig. 8, and Supplementary Material Fig. A3). However, owing to the exponential dependence of dissolution rate on T , the topology of the dissolution curves (e.g. Supplementary Material Fig. A3) can be fitted by a concave-down exponential and include a long delay at lower temperature followed by a rapid collapse of zircon size at peak temperatures. In other words, it is the highest temperature that matters; the prehistory of temperature increase matters much less.

Linear temperature increase followed by symmetrical temperature decrease

Figure 9 presents a case of a symmetrical temperature history: heating to the liquidus leading to zircon dissolution, followed by cooling to the solidus and zircon growth. Different cell sizes are modelled with zircon completely dissolving in the largest cells and partially dissolving and achieving some minimal size in smaller cells. This simulation illustrates that once zircon fully dissolves and Zr diffusively equilibrates throughout the cell, it takes longer for zircon to recrystallize from the melt to the same original size within the same original melt cell volume. This result is not intuitive and implies a non-symmetrical nature of dissolution then growth to regain the same size after a return to the original conditions following a heating event.

Temperature evolution inside and outside cooling dikes and sills

As this study considers crustal melting and magma crystallization histories via surviving and crystallizing zircons, it is necessary to consider the temperature–time history of the rock inside and outside a cooling igneous body. Sill and dike intrusions are critical in delivering heat and maintaining elevated temperature in the host-rock (Annen & Sparks, 2002; Dufek & Bergantz, 2005). The position of the zircon cell volume inside or outside a sill, combined with a specified phase diagram (T – X diagram), permits monitoring the progress of zircon dissolution and subsequent growth, or lack of these

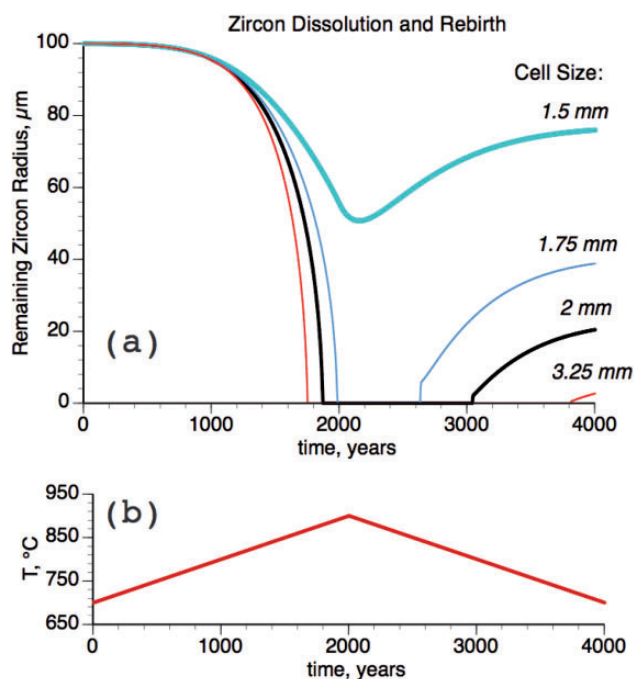


Fig. 9. Zircon dissolution and rebirth with a $0.1^{\circ}\text{C a}^{-1}$ temperature rise within variable melt cell volumes at original undersaturation $\Delta U=0$. M factor varies as a function of T as in Fig. 4b. It should be noted that zircon size history is not symmetrical (a), despite a symmetrical temperature history (b), as zircon growth is slower after diffusive dispersal of Zr into the far field of the melt cell. Zircon in small melt cells (1.5 mm) will not fully dissolve and preserves the core, whereas larger melt cell sizes promote later nucleation of zircon. Zircon will eventually regain its original size but after longer time of diffusive growth at lower T .

if conditions are not met. A heat wave propagating from a sill with initial temperature T_d into country rocks with temperature T_c will pass through each coordinate point perpendicular to the sill with decreasing peak temperature and increasing wavelength with distance from the sill (Fig. 10; Supplementary Data Fig. A3). Outside the sill the highest temperature peak, equivalent to the half-temperature $(T_d - T_c)/2$, is realized at the contact between the sill and the country rocks. At this boundary, zircon dissolution starts almost instantaneously after sill emplacement. Distances $x=10\text{--}10^2\text{ m}$ away from the sill will be heated at time $t\sim x^2/k$, where k is the thermal conductivity, $\sim 0.6 \times 10^{-6}\text{ cm}^2\text{ s}^{-1}$ (Carslaw & Jaeger, 1959). Partial melting of the country rocks in these areas creates conditions for zircon dissolution, but often with a delay of $10^2\text{--}10^3$ years (Fig. 10) after the arrival of the heat wave. The $T\text{--}t$ histories around conductively cooling dikes and sills of a certain half-width h at distance coordinate x from the sill center are given by the analytical solution of Crank (1975):

$$T = \frac{(T_d - T_0)}{2} \left[\operatorname{erf}\left(\frac{h-x}{\sqrt{kt}}\right) + \operatorname{erf}\left(\frac{h+x}{\sqrt{kt}}\right) \right]. \quad (12)$$

Figure 10 illustrates temperature profiles around a cooling 950°C , 100 m thick sill showing the temperature histories of zircon cells at varying distances from the sill

center. The melting and latent heat sink (Stefan problem) is not taken into account here for simplicity and melting will shorten the width of the heat wave. For relatively small melting degrees, conduction will still dominate. Temperature–time histories were monitored at three points: (1) inside the sill, aimed at modeling the dissolution of zircons captured from the country rock; (2) at the contact; (3) at a distance from the sill in rocks that undergo small-degree partial melting. The survivability of zircons, as well as the amounts of dissolution and subsequent rim growth, are different in these three positions (Figs 11–13) and are obviously strongly dependent on the temperature and the thickness of the sill as well as the country-rock temperature.

In our modeling we experimented with sills of thickness varying from 10 to 900 m with $T=950\text{--}1300^{\circ}\text{C}$ intruded into country rocks at $450\text{--}750^{\circ}\text{C}$; most runs were done considering subsolidus $<650^{\circ}\text{C}$ country rocks. We have also computed the rates of cooling and heating of single zircon cells at different positions relative to the sill (Supplementary Material Fig. A3). For a short period of several years internal and external contact zones, adjacent to the contact, undergo dT/dt variations greater than 2°C a^{-1} . As we already explored in Fig. 8, even at high temperature this amount of time is insufficient to cause significant dissolution of any except the smallest zircons. Most zircons will thus experience dissolution–reprecipitation processes over a more prolonged heating–cooling duration and $dT/dt < 1^{\circ}\text{C a}^{-1}$.

Zircon dissolution and survival inside and outside intruded dikes and sills

Zircon dissolution, core survival, and regrowth in Zr-undersaturated sills depends on the timescales of their cooling (Fig. 10). The progress of dissolution depends on the duration at each changing temperature step as the diffusion coefficient and C_{sat} are temperature dependent. Zircons of $40\text{--}100\text{ }\mu\text{m}$ radius provide good marker points for the dissolution of the median to the largest zircon sizes within a population. The rock cell size around each zircon was $0.7\text{--}1.7\text{ mm}$, which was computed based on observed zircon sizes (Table 1) and constant whole-rock Zr concentrations, for which we chose 220 ppm total Zr for country rocks and 110 ppm for the intruded sill. This choice assumes that Zr concentration doubles upon cooling and 50% crystallization of an originally 950°C silicic sill when it reaches thermal equilibrium with the country rocks, assuming that the crystallization T relationship (Fig. 4c), or generic liquid line of descent, is the same for the sill and the country rocks. This is analogous to silicic magma accumulation zones in which different batches of zircon-saturated liquids stall, crystallize, give up heat, and undergo $\sim 50\%$ differentiation (e.g. Bea, 2010).

The $T\text{--}t$ history of each melt volume inside and outside the sill may have four outcomes: (1) all zircons of a certain size dissolve completely and never reprecipitate; (2) zircons dissolve completely but reprecipitate (e.g.

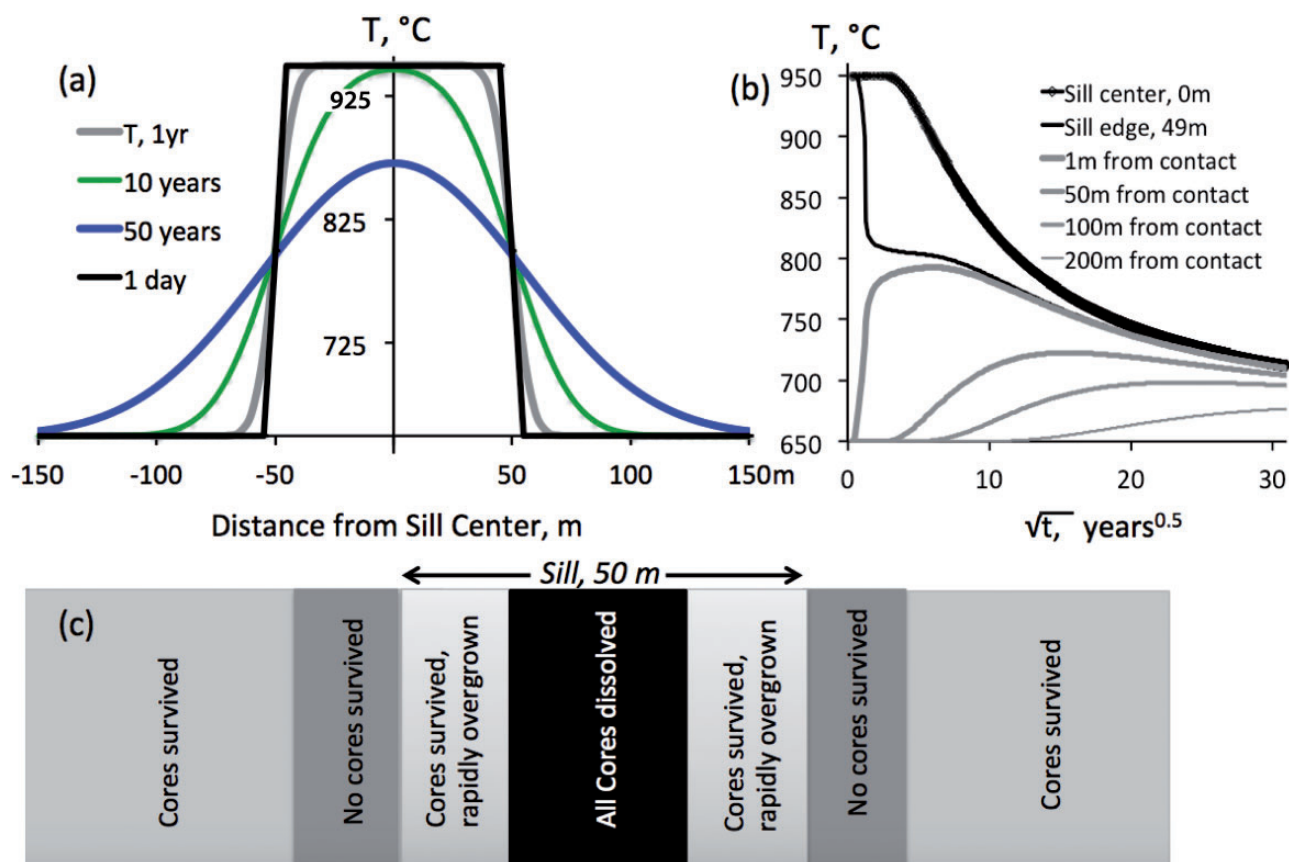


Fig. 10. Zircon dissolution inside and outside a 950°C, 100 m sill emplaced into 650°C country rocks. Temperature evolution is based on conductive cooling, after Crank (1975). Computed temperature–time paths for indicated coordinates inside (upper two curves) and outside (the other curves) the sill. Three zones inside the sill and two zones outside the sill are shown. Inside the sill, inherited zircons are variably dissolved then overgrown on timescales of sill cooling; in the proximal country rocks all zircons dissolve and are replaced by newly precipitated zircon; further away zircon cores survive. Figures 11–14 illustrate the zircon destinies inside the sills and in the country rocks in different parameter space.

Fig. 9; Supplementary Data Fig. A4) leaving no inherited cores and resetting U–Pb, O, and Hf isotopic compositions as well as trace element signatures; (3) zircons partially dissolve, but are overgrown by a new rim with the isotopic and chemical characteristics of the new melt, leaving behind zircons with inherited cores; (4) zircons are minimally affected during heating owing to its short duration or the small magnitude of the temperature perturbation and no rim growth occurs.

Zircon dissolution–reprecipitation within a dike or sill

Figure 11 presents modeling results for $\bar{R} = 40 \mu\text{m}$ zircon dissolution inside a 0.74 mm cell with $\Delta U = 100$ ppm Zr undersaturation corresponding to a bulk-rock Zr concentration of 120 ppm. This rock cell with a zircon in the center is then placed in different positions inside a sill of given thickness. The following observations can be made: (1) sills will dissolve zircons in their slowly cooled interior only when there is sufficient time for dissolution to occur, whereas the rapidly cooling contact zones of the sill (or dike) will cool too rapidly for zircon to dissolve; (2) the proportion of interior sill thickness with complete zircon core obliteration

increases as the square root of sill thickness. Sills thinner than 10 m half-thickness will dissolve only the outer 1 μm of typical zircons; sills with 50 m half-thickness will completely dissolve 30% of the zircon external radius. Sills with a >200 m half-thickness will be able to dissolve 30–35 μm , or 80% of the external radius of zircons within 4/5 of the sill's interior on timescales of their cooling. Inside thicker sills, zircons with radii $\bar{R} = 40$ and 100 μm dissolve rapidly in 16 and 19 years, respectively, regardless of the size of the sill. This suggests that for thick sills it is the kinetics of zircon dissolution at high temperature and at given undersaturation that controls the dissolution time, not the sill cooling timescale. For thinner sills, the main control on zircon dissolution is the rate at which the sill cools.

Zircon dissolution–reprecipitation in country rocks heated conductively by a dike or sill

Next, we place the same zircon cell with $\Delta U = 0$ (thus in C_{sat} condition at 650°C) outside the sill (Fig. 12) to observe the dissolution then growth process as the heat wave passes. Modeled zircon survivability shows the same simple relationship of sill thickness vs distance from the sill (Fig. 12) and rapid transitions from

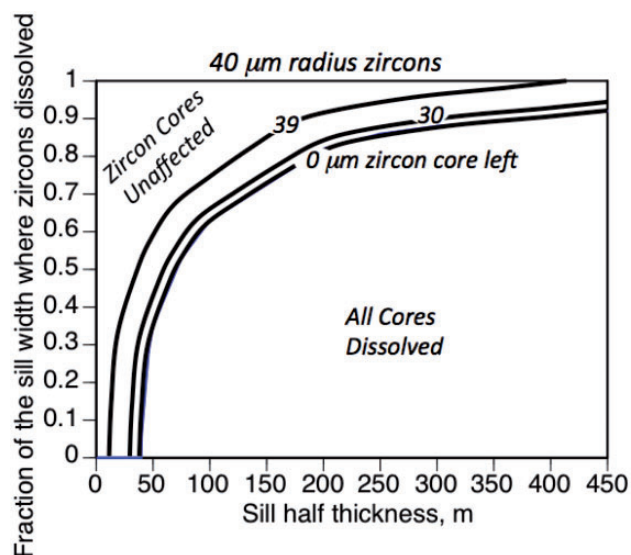


Fig. 11. Numerical results for dissolution of $\bar{R} = 40 \mu\text{m}$ zircons inside a cooling, originally 950°C sill of variable thickness; the vertical axis denotes the fraction of the sill in which zircons are dissolved to sizes indicated. The rapid transition from unaffected to completely dissolved zircons, and that even small 50 m half-thickness sills are capable of dissolving zircons, should be noted.

complete dissolution to minimal change as in the sill interior. Zircon dissolution time, however, is always long and is controlled by the temperature history of each dissolving zircon inside a melt pocket (Figs 9 and 10). Thin sills will produce smaller and shorter heat spikes than thicker ones. Zircons in areas 100 m away from a 300 m thick sill will start dissolving only ~ 500 years after sill intrusion, and zircons reach minimum size in 3000 years before starting to regrow. This situation is analogous to the influence of the Basistoppen Sill on the Sandwich Horizon in the Skaergaard Intrusion, Greenland, 100 m away (Wotzlaw *et al.*, 2012), dated by ID-TIMS to have experienced a geochronologically recognizable several thousand years delay of dissolution after Basistoppen intrusion.

An increase in sill temperature obviously increases the zone of complete dissolution of zircons in the country rocks, and this relationship is a simple linear function of sill half-thickness (Fig. 13). Thick (>200 m) sills are capable of obliterating zircons (thus erasing their U–Pb geochronological and isotopic information) at a comparable distance to their own thickness in a realistic 0.7 mm cell. The farthest areas will experience zircon dissolution many thousands of years after sill intrusion. This observation predicts a spatial distribution of ages younging outside the sill for many thousands of years, a timescale that is now resolvable by ID-TIMS. This should set up limits for dating thermal ‘episodes’ using zircons that can be treated as ‘periods’ lasting thousands of years (see below and Supplementary Data A4). Spatial distributions of ages in the field and their recognition in accordance with our simple theory may also set up a natural test for future geochronology efforts.

Sill intrusion into country rocks of different temperature

We also modelled sills with half-thicknesses of 100 m, a constant temperature of 1200°C , but variable initial country-rock temperatures between 450 and 650°C (Fig. 14), representing environments ranging from cold hydrothermal systems to the lower or mid-crustal wet granite solidus. We used the same $40 \mu\text{m}$ zircons within the large 1.5 mm and the small 0.7 mm cells used above. Diffusion was allowed to proceed even at the lowest temperature, assuming zircon was always surrounded by a sphere of melt at the temperature of the country rocks. As the lowest (450 – 550°C) temperatures are below the granitic eutectic, the interstitial melt can be imagined as an interstitial pegmatitic–hydrothermal solution, which can exist at such temperatures (Tuttle & Bowen, 1958; Lundstrom, 2009), although the rates of dissolution are negligibly small on the short timescales of heat wave migration at these low temperatures. For simplicity, we avoided bulldozing effects and major minerals were considered to contain microzircons and $K_{\text{Zr}} = 1$; thus partial melting did not cause an additional undersaturation with respect to Zr.

For 1.5 mm diffusion cells, zircon dissolution proceeds far away from the sill, and the dependence of the size of the zircon obliteration zone on country-rock temperature is exponential. The 450°C rocks have a 13 m zone next to the sill with obliterated zircons; at 600°C this zone expands to 140 m, and the hottest (650°C) country rocks lose zircons 600 m away from the sill. The last requires up to 25 kyr after sill intrusion to occur. The peculiar feature of zircon dissolution in the larger 1.5 mm cell is the lack of new zircon nucleation over long (30 kyr) durations (e.g. Fig. 9). For 0.7 mm cells, dissolution proceeds over a correspondingly smaller distance from the sill, about half that of the 1.5 mm cell, also with an exponential dependence on rock temperature (Fig. 14). We conclude that country rocks with incipient Zr undersaturation (greater cell sizes with the same zircon size in the middle) can lose zircons by heat conduction from a relatively small sill.

Effects of major mineral crystallization, bulldozing, and precipitation of microinclusions of zircon

In this study we implemented a boundary condition with two independently moving boundaries (Fig. 3), which permits exploration of the effect of major phase crystallization on Zr concentration inside the shrinking or expanding melt cell volume, and of kinetically induced Zr enrichment on the outer boundary.

Volumetric effects of major phase crystallization

Crystallization of major phases effectively shrinks the cell size and thus the melt volume available for Zr diffusion towards the growing crystal. Because of the cubic relationship between the volume of a sphere and its radius, this influence on zircon cell size is insignificant:

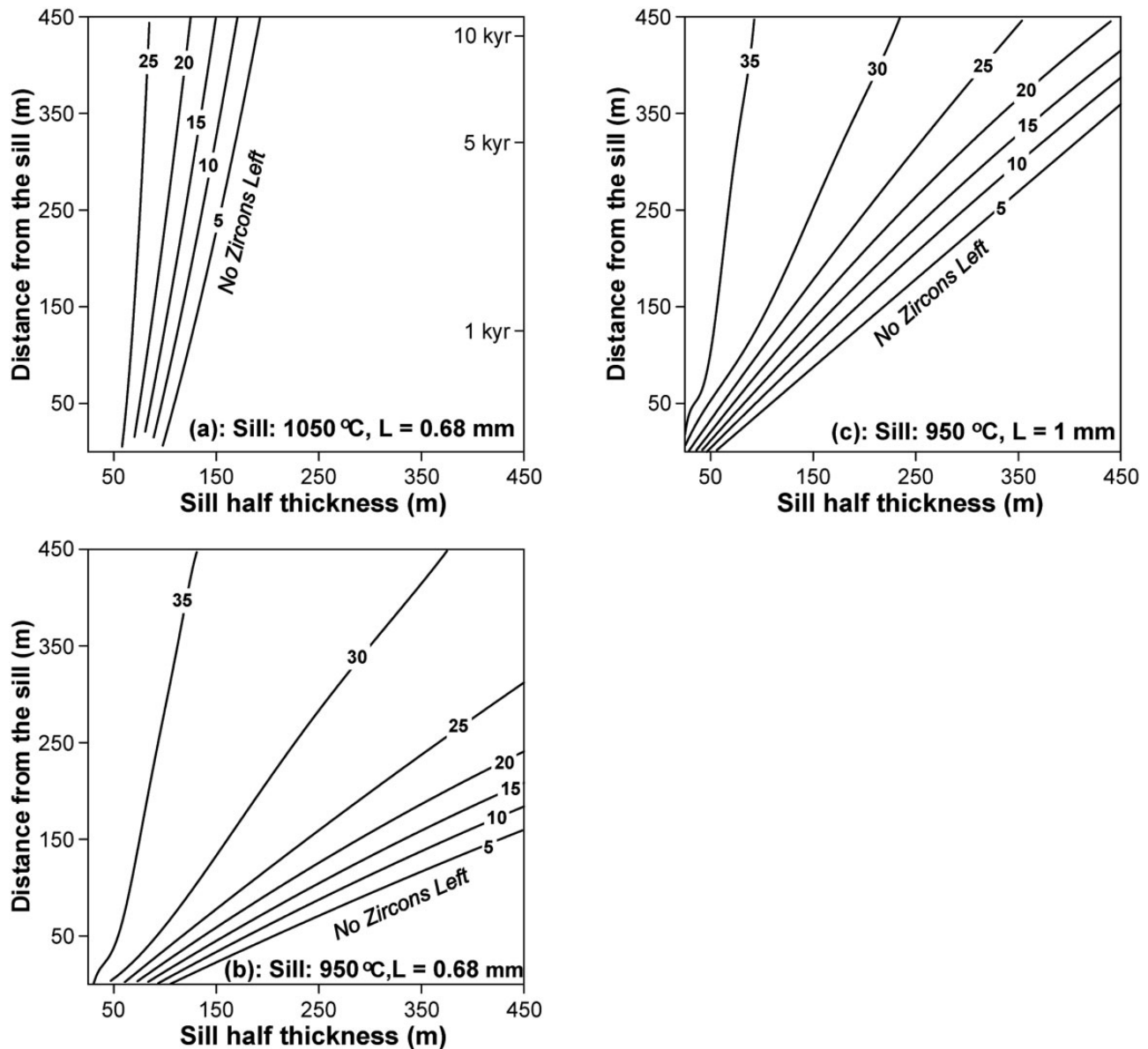


Fig. 12. Numerical results for dissolution of $\bar{R} = 40 \mu\text{m}$ zircon in the contact aureole of a conductive dike or sill of a given thickness and temperature. Minimum zircon radius is shown by contour lines; L is melt cell size. In (a), tick marks on the right-hand vertical axis show years to complete dissolution.

50% volume crystallization of the outer radius is only 11% of the sphere's outer radius, and thus diffusion distance. Conversely, 99% inward volume crystallization leaves 13% of the radial distance, corresponding to 1% melt volume around the zircon. Such relationships permit modeling of very low degrees of crustal melting around typical 10–100 μm radius zircons inside 0.3–3 mm wide cells (Fig. 2).

The main influence of crystallization is to increase Zr concentration in the melt, thus changing Zr saturation conditions inside the cell. At small degrees of 10–20% crystallization these compositional changes are less significant, but the large temperature change at this crystallinity has a large effect on C_{sat} (Fig. 4). However, major phase crystallization effects are dramatic for the

greater crystal percentages at lower T (e.g. near the eutectic) realized in subvolcanic plutonic rocks and migmatites. Near the eutectic, changes in T are insignificant relative to changes in crystallinity, thus C_{sat} conditions and Zr concentration in the melt do not change much owing to temperature, but may change significantly owing to melting or crystallization of Zr-free or Zr-poor major phases. Upon heating, the melt boundary of the cell retreats, leaving behind a Zr-free, high M -factor melt (Fig. 3) that surrounds the zircon with its C_{sat} melt shell $s < r < R$ (Fig. 3); this melt will have zero Zr concentration in the initial melt, which will also have a higher M factor, capable of greater solubility of Zr. Such a nearly isothermal, eutectic scenario will result in conditions of almost unlimited radial Zr diffusion into an

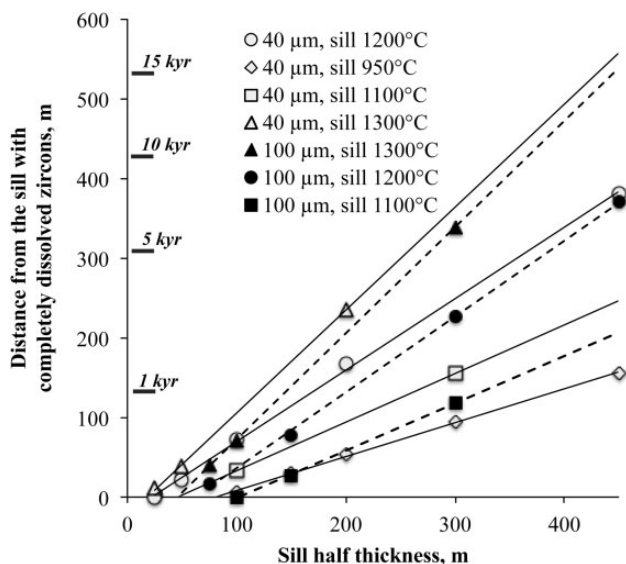


Fig. 13. Thermal effect of sills of various thickness and temperatures on zircon survival in country rocks containing 40 and 100 μm radius zircons. Tick marks on vertical axis show years to complete dissolution. The simple, nearly linear relationships should be noted.

infinite space from the dissolving zircon, leading to its accelerated disappearance. The additional effect of the major phases on zircon survival and the diffusion conditions around them is through compositional and M -factor variations that accelerate or decelerate zircon dissolution and growth (Fig. 4b).

Kinetic effects

The advancing or retreating outer crystal melt boundary with rate W (Fig. 3) may 'bulldoze' in high concentrations of Zr that will affect the Zr diffusion profile and thus zircon growth or dissolution histories. Upon rapid crystallization, our numerical model predicts significant increases in Zr concentrations owing to major phase crystallization (Fig. 15; Supplementary Material Fig. A3). Watson & Muller (2009) additionally considered the effects of trace element partitioning into zircon owing to non-equilibrium crystallization. As our model does not implicitly consider zircon nucleation, to create the appearance of zircon microinclusions inside major phases we set up an increased bulk partition coefficient $K_{\text{Zr}} = (\text{major phase with 0 ppm Zr plus zircon microinclusions with 490,000 ppm Zr}) / (\text{concentration of Zr melt})$. The choice of K_{Zr} can be governed by the $\Delta C = C_{\text{sat}} - \Delta U$ concentration of Zr in the bulldozed outer zone, to keep it from kinetically increasing to 'unreasonably high' concentrations defined by the user. It is unrealistic, for example, to expect Zr oversaturations to exceed tens of ppm without nucleation (e.g. Bacon, 1989).

Our modelling demonstrates that cooling rates of $0.1\text{--}1^\circ\text{C a}^{-1}$ characteristic of 950°C dikes and sills intruded into 650°C rocks (Supplementary Material Fig. A3) generate significant bulldozing effects. Such cooling rates correspond to maximum major mineral growth

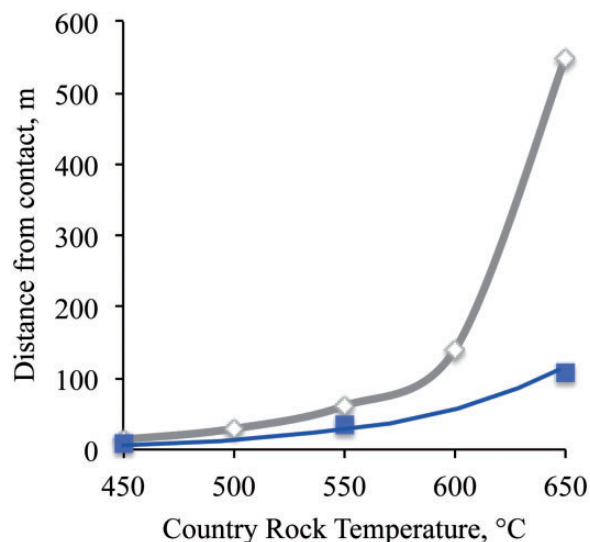


Fig. 14. Effect of country rock temperature on zircon survival owing to the heat wave propagating from a 200 m thick sill with a temperature of 1200°C . It should be noted that hotter country rocks experience zircon loss at a greater distance. The lower curve is for a zircon cell radius of 0.7 mm and the upper curve is for a 1.5 mm radius.

rates of $0.5 \text{ vol. } \% \text{ a}^{-1}$ in our model. However, numerical experimentation with a 600 m sill intruded into hotter (750°C) rocks is characterized by much slower cooling rates of the order of $0.01\text{--}0.04^\circ\text{C a}^{-1}$ and there are no bulldozing effects. Such cooling rates result in $0.04 \text{ vol. } \% \text{ a}^{-1}$ major mineral crystallization. Zircons grow to the same size whether at $K_{\text{Zr}} = 0.01$ or 1. Values of K_{Zr} in the range of $0.1\text{--}0.3$ are most appropriate for realistic cooling rates, and $K_{\text{Zr}} = 0.9\text{--}1$ for the most extreme cases of rapid cooling and major mineral bulldozing effects.

Other accessory minerals

We have also performed analogous modeling with other accessory minerals for which solubility and diffusion have been determined: apatite (Harrison & Watson, 1984), rutile (Ryerson and Watson, 1987), and monazite (Rapp & Watson, 1986); the results of these models are presented in Fig. 16. Separate code lines are included in the MATLAB program in the Supplementary Material. Whereas dissolution of monazite and apatite into an infinite volume of melt with maximal undersaturation is more rapid in equivalent conditions to those for zircon (owing to the slower diffusion coefficient of the latter), dissolution in a cell of identical size is comparable, because it is primarily determined by the kinetics of the temperature increase, rather than by each of the rates of diffusion of Zr, P, and rare earth elements (REE) into infinite space. Given the usually large sizes of apatite compared with zircon, dissolution in limited cells may in theory lead to equal or even better preservation of apatite compared with zircon. Again, it is the cell size and saturation conditions within the cell that determine the relative survivability of accessory minerals. We notice that experimentally

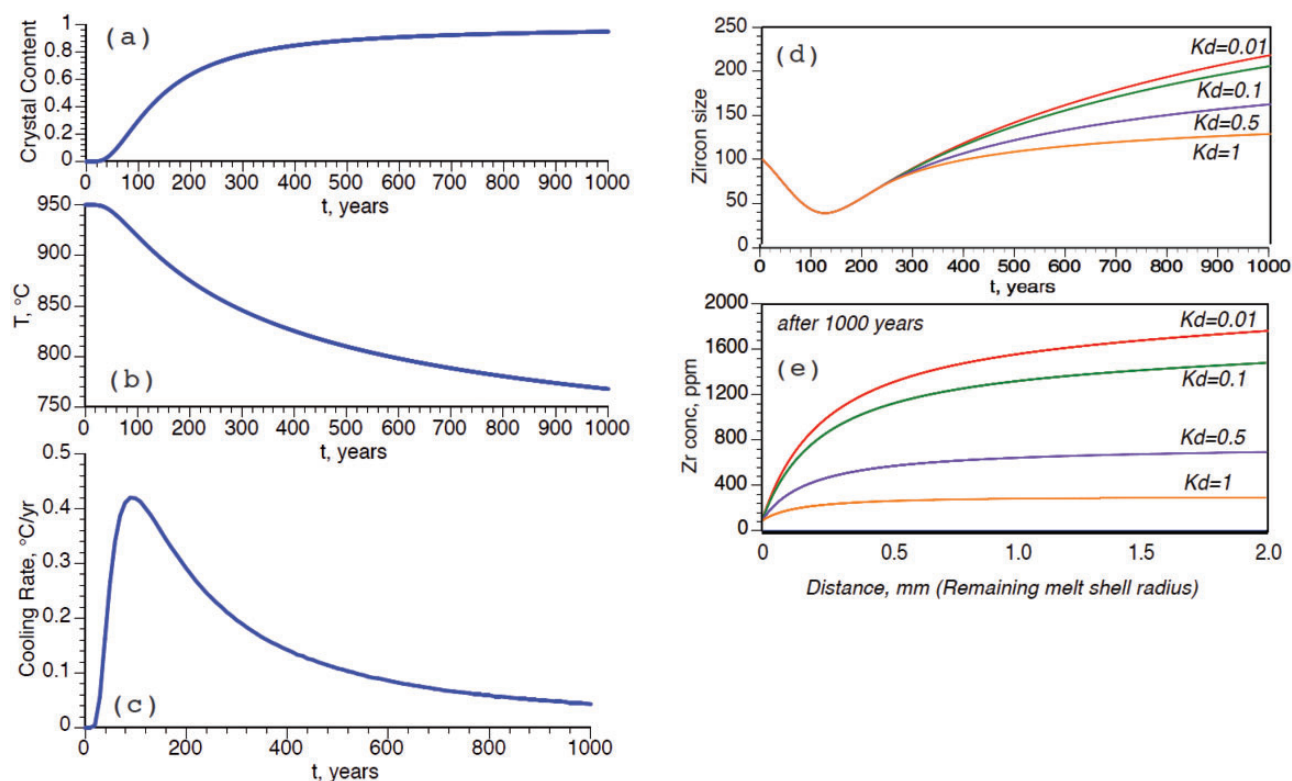


Fig. 15. Bulldozing effects of major phase crystallization on Zr concentration and growth rate of zircon inside a 5 mm cell. Zircon of originally 100 μm radius is captured in the center of a 200 m, 950 $^{\circ}\text{C}$ sill with zircon undersaturation $\Delta U = 100$ ppm. (a–c) Crystal content, conductive cooling history and cooling rate of the sill for 1000 years. (d) Evolution of zircon radius for different bulk partition coefficients of Zr between major minerals and melt. The initial dissolution of zircon owing to original Zr undersaturation of the melt, followed by growth inside the cell, should be noted. (e) Concentration profiles of Zr between zircon (left boundary) and major mineral (right) moving boundaries. It should be noted in (d) and (e) that if major minerals do not take Zr ($K_{Zr} = 0.01$; lack of microzircon nucleation), significant Zr enrichment occurs near the right boundary that leads to accelerated zircon growth.

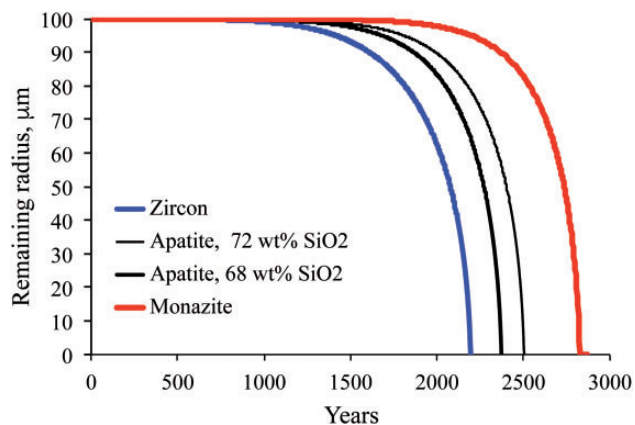


Fig. 16. Dissolution of 100 μm zircon, apatite, and monazite in silicate melt of different SiO_2 content with 3 wt % H_2O during 0.1 $^{\circ}\text{C}$ T rise from 650 $^{\circ}\text{C}$ to 950 $^{\circ}\text{C}$. Cell size is 1.5 mm.

determined diffusion coefficients for P, Y and REE, compared with Zr, exhibit large variations in activation energies (Rapp & Watson, 1986) and the choice of diffusion coefficient sometimes determines the outcome, especially when propagated to a lower T range. New and better controlled lower T (700–800 $^{\circ}\text{C}$) diffusion experiments are required.

Other factors influencing zircon dissolution

We next briefly discuss other factors that can modify zircon dissolution rates. Although we investigated conductive regimes of heat transfer, convection in sills will have a limited influence in accelerating zircon dissolution. Convection raises sill contact temperatures to higher than the half-difference $(T_d - T_c)/2$ between the magma and the country rocks in contact (Fig. 10b), proportional to the intensity of convection and the Nusselt number (Huppert & Sparks, 1988). Convection also keeps T_d more uniform throughout the sill, but the overall duration of the high dT/dt regime is shorter, providing little enhancement of zircon dissolution. Convection in sills, and its effect on maintaining higher temperature in the interior, can be envisaged from the numerical experiments of Bea (2010) and Simakin & Bindeman (2012). The latter presented data for thin convective 7–30 m thick sills, and when compared with heat conduction from sills of equivalent size this demonstrates a factor of ~ 1.5 more rapid initial temperature drop inside the sill during convection, followed by the cessation of convection and prolonged conduction in a crystal-locked state (Bea, 2010). On the outside of the sill, the convective rise of the contact temperature is short-lived. Thus, convection leads to little or no enhancement of zircon dissolution, but it does play an important role in

mixing zircons with different dissolution histories and isotopic compositions together within a cooling sill or a magma body (e.g. Bindeman & Simakin, 2014).

Another factor is the relative motion of melt and zircon that sharpens diffusive gradients and may theoretically accelerate their growth or dissolution. The process can be scaled through the Peclet number $Pe = VL/D$ times the melt viscosity (Levich, 1962). The analytical solution of Levich (1962) for the formula to be valid and cause advective acceleration of dissolution is for Pe greater than ~ 1 . For zircon sinking in a silicic melt with a viscosity of 10^6 Pa s, typical zircons with $\rho = 4.6$ g cm $^{-3}$ and $\Delta\rho = 2.3$ g cm $^{-3}$ and radii of 40 and 100 μ m will experience Stokes settling of 1.1 and 6.9 mm a $^{-1}$ (10^{-9} and 5×10^{-8} cm s $^{-1}$), with a Peclet number of < 1 , insufficient to make any difference. Because of the slow diffusion of Zr in the melt (10^{-12} cm 2 s $^{-1}$), sinking therefore plays an insignificant role in zircon dissolution–crystallization.

Implication for precise U–Pb geochronology

Our models for zircon dissolution and recrystallization presented above suggest new directions for improving geochronology, isotopic and trace element studies of zircon. Chemical abrasion ID-TIMS methods (Schoene & Schmitz, 2007; Schaltegger *et al.*, 2009) target single or partial zircon grains and often rely on the six to eight youngest grains to record the last magmatic episode, whereas older grains (which are impossible to date with sufficient precision by *in situ* U–Pb ion microprobe methods) are called antecrysts or xenocrysts. U–Th methods for the youngest grains permit high-precision *in situ* analyses (Charlier & Zellmer, 2000; Storm *et al.*, 2011; Carley *et al.*, 2011; Stelten *et al.*, 2015).

Figure 17 and Supplementary Material Fig. A4 show the results of bulk U–Pb age evolution in the case of complete zircon dissolution followed by growth at different distances from a sill over the conductive cooling timescale of a 500 m thick sill with either 950°C or 1200°C initial temperature, for natural timescales of their cooling in 650°C country rocks. At distances ranging from 10 to 500 m from the sill, an initial 40 μ m radius zircon will completely dissolve, but new zircon will reappear after 12–16 kyr as the partially molten rock cools below zircon saturation. Although theoretically zircon should grow to the original zircon size of 40 μ m within each cell, the last 2–3 μ m outer radius will take an exceedingly long time owing to decelerating cooling rates, and if other crystallizing minerals take up some Zr (Fig. 3) the zircon may remain permanently smaller.

We plotted zircon age since its regrowth and observe a nearly linear relationship of age versus the percentage of crystallized zircon volume (double-angled lines in Fig. 17), and compare these with *in situ* dates by U–Th disequilibrium methods for cores and outer rims of zircons reported by Stelten *et al.* (2015) for three young Yellowstone lavas. These lavas (Grants Pass, West Yellowstone and Pitchstone Plateau) erupted sequentially

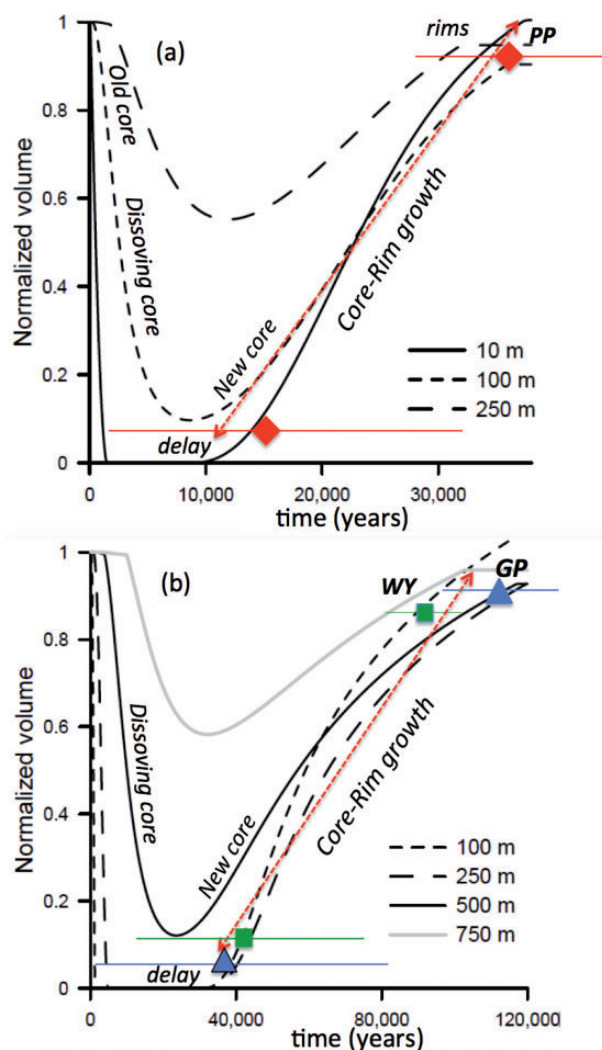


Fig. 17. Progress of dissolution, then volumetric crystallization of zircon in 650°C country rocks at different distances from the sill outer boundary (10–750 m) upon passage of a conductive thermal wave from 250 m half-thickness, 950°C (a) and 1200°C (b) initial temperature sills. Continuous and dashed line trajectories denote dissolution then regrowth of single zircons; the rapid dissolution of zircons followed by nearly linear (double-angled line) growth of zircon volume vs time should be noted. PP (Pitchstone Plateau, diamonds), WY (West Yellowstone, squares) and GP (Grants Pass, triangles) are zircon core and rim ages from young Yellowstone lavas dated by U–Th *in situ* methods (Stelten *et al.*, 2015). Core–rim age difference is indicated on the model curves, each requiring host melt crystallization (Fig. 4c) by $> 50\%$ after thermal rejuvenation by the sill. (See text for discussion.)

between 118 and 75 ka from approximately the same area in the Yellowstone caldera along its western lineament, and contain zircon rims with ages identical to the eruption age and cores with ages that are offset by tens of thousand of years (Stelten *et al.*, 2015, table 5). Stelten *et al.* interpreted these zircons as antecrysts inherited from a single caldera-wide, evolving crystal mush requiring no thermal perturbation (as their other data seem to show). We notice in their data, and earlier datasets of Vazquez & Reid (2002) and Watts *et al.* (2012), that most

of the zircon volume in each lava is U–Pb rejuvenated and is of eruption age, and that the core age is offset from that of the rims by a fixed amount; both cores and rims become progressively younger in each successive lava. A possible alternative explanation is that each of these lava flows represents punctuated sequestration of melts, in which the parent magma (progressively more differentiated magma or mush) of each earlier lava flow is parental to the subsequent magma batch with rejuvenated zircons. Figure 17 tests this possibility and demonstrates that an incrementally intruded (e.g. Annen & Sparks, 2002) 500 m thick hot sill ('hot plate') is capable of not only rejuvenating the pre-existing crystal mush or solid rock in the required proportions, but does so robustly above zircon saturation to at least 850°C, as required by phase equilibria (Almeev *et al.*, 2012), and high oxygen isotopic temperatures (Loewen & Bindeman, 2016). Thinner and cooler sills will induce less remelting and preserve some zircon inheritance further from their contact. The subsequent cooling and crystallization of sequestered high-degree melts will proceed to >50%, reach zircon saturation and generate the observed zircon core–rim relationships observed by Stelten *et al.* (2015).

The modeling summarized in Fig. 17 also demonstrates that upon complete dissolution and continuing cooling, new crystallization of zircon will be delayed for up to 10–30 kyr, erasing any xenocrystic memory, but then zircon will reappear and grow with a nearly linear dependence of volume with time (Fig. 17, Supplementary Material A4). If dated by ID-TIMS methods, its average age will be an integral of this linear function after a delay. Although zircon air abrasion is now almost an abandoned practice, we recommend performing it on zircons prior to ID-TIMS dating to obtain even better resolution of the zircon crystallization interval and to determine the slope. Running large and small zircons (e.g. Charlier & Zellmer, 2000) and consideration of details of zircon CSD (e.g. Simakin & Bindeman, 2008) should also become a common practice. Given the simple linear relationship observed, a small crystal, bulk separate and an abraded core of a large crystal should allow simple reconstruction of the age–volume relationship and thermal history of a rock.

Diffusion profiles around dissolving grains

We used our code to model the measured Zr concentrations in glass around an 80 µm zircon from the Yellowstone Summit Lake flow [Fig. 18; see Loewen & Bindeman (2015) for data and petrological context]. The increase in Zr concentration close to the zircon boundary demonstrates the preservation of a quenched dissolution profile around the zircon. Given diffusion distances, the heating event that caused this dissolution lasted only several months and requires a pre-eruptive magma temperature increase of 13°C. To be preserved an eruptive quench lasting <0.05 yr is required; the heating even can be speculated to be a pre-eruptive injection of new magma that may have acted as an

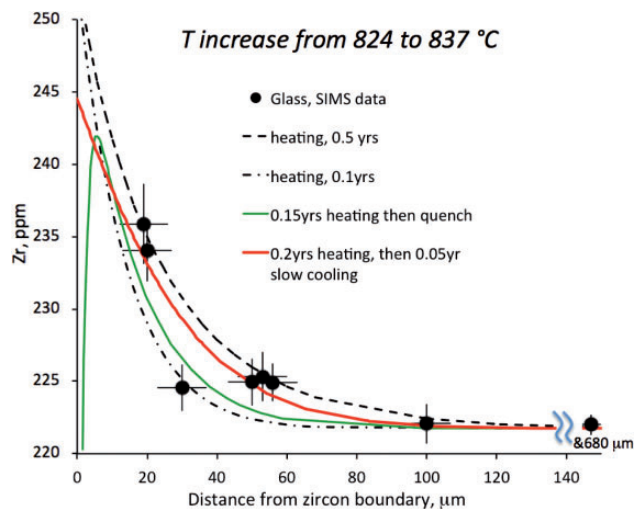


Fig. 18. Ion microprobe (secondary ion mass spectrometry) profile (15 µm spot size) across rhyolite glass from a zircon crystal in the Summit Lake flow of Yellowstone (sample YS08-05, Loewen & Bindeman, 2015) and model curves (this work). Higher concentrations of Zr in the vicinity of the boundary suggest that zircon was dissolving for 0.1–0.5 years before the eruption and that this dissolution profile was quenched by the eruption, probably as a result of cooling and rapid water loss upon emplacement, leading to a rapid decrease in water-dependent Zr diffusion coefficients and a rapid drop in Zr diffusion rates (by two orders of magnitude, Zhang *et al.*, 2010), which is essentially equal to an equivalent temperature drop of 100°C, in accordance with equation (1) in the text.

eruption trigger. This natural documentation of preserved profiles in glass around dissolving zircon creates a tool for learning about timescales of magmatic processes that can be directly modelled using the code presented here. Given sometimes thin (tens of microns) profiles, the use of NanoSIMS may be required to resolve details in the ~5–10 µm distance range around a dissolving crystal, and in particular a peak in Zr concentration related to temperature change (Fig. 18).

CONCLUDING REMARKS

Our modeling captures the main features of zircon behavior upon crustal melting through cycles of dissolution–nucleation and growth, and we observe a wide and quantifiable range of controls and outcomes that can be of practical use and predictive value for user-specific situations.

1. Approximation equations (10) and (11) predict lifetimes of zircons of different size as a function of temperature and Zr undersaturation.
2. Elementary cell size has fundamental significance in the survivability of zircon and other accessory minerals. For a given cell size, even mild temperature fluctuations in Zr-undersaturated rocks (e.g. amphibolites) lead to zircon disappearance and no new growth upon cooling; likewise, zircon in Zr-oversaturated rocks (gneisses) will experience overgrowth upon melting.

3. Dissolution of other accessory minerals, such as apatite and monazite, which contain slow-diffusing 3+ and 5+ elements with low saturation levels, indicates comparable lifetimes upon heating that are controlled by the cell sizes and temperature histories of the rock, to a far greater extent than relative diffusion differences between the constituent elements of these minerals.
4. Consideration of temperature histories in and around cooling dikes and sills predicts alternating areas of complete disappearance of cores and areas where cores survive and are overgrown by rims. As zircons inherit their O and Hf isotopic compositions from their immediate melt cell, even a single thermal episode can generate isotopic diversity in a zircon population.
5. Zircon ages become younger away from the sill as the heat wave propagates, resetting ages sometimes with a delay of 10^3 – 10^4 years after sill intrusion. We observe a simple near-linear increase of zircon volume with age of crystallization, resulting from conductive cooling timescales; this should allow two-point determination of cooling duration by *in situ* or ID-TIMS methods on cores and rims of zircon.
6. For zircon-rich rocks, only the largest (>200 μm) igneous bodies are capable of complete dissolution–reprecipitation of typically sized zircons at significant distances from the intrusion. In contrast, Zr-poorer rocks may lose zircons many diameters of the sill away. Smaller intrusions result in partial dissolution and rim overgrowth.
7. Co-crystallization of surrounding major minerals provides accelerating effects on zircon growth owing to the bulldozing effect of Zr. Large Zr oversaturation on the boundary may result in microzircon crystallization, leading to a large effective Zr partition coefficient for the major mineral.

FUNDING

NSF EAR EAR/CAREER0844772 and the University of Oregon Meierjurgun fund supported this research.

SUPPLEMENTARY DATA

Supplementary data for this paper are available at *Journal of Petrology* online.

ACKNOWLEDGEMENTS

We thank Matt Loewen, Dylan Colón, Antonio Acosta-Vigil, Jörg Hermann and two anonymous reviewers for careful and insightful internal and external reviews and editorial comments.

REFERENCES

Acosta-Vigil, A., London, D., Morgan, G. B., VI, & Dewers, T. A. (2006). Dissolution of quartz, albite, and orthoclase in H₂O-

- saturated haplogranitic melt at 800°C and 200 MPa: diffusive transport properties of granitic melts at crustal anatectic conditions. *Journal of Petrology* **47**(2), 231–254.
- Acosta-Vigil, A., Buick, I., Hermann, J., Cesare, B., Rubatto, D., London, D. & Morgan, G. B. VI, (2010). Mechanisms of crustal anatexis: a geochemical study of partially melted metapelitic enclaves and host dacite, SE Spain. *Journal of Petrology* **51**(4), 785–821, doi:10.1093/petrology/egp095.
- Almeev, R., Bolte, T., Nash, B., Holtz, F., Erdmann, M. & Cathey, H. (2012). High-temperature, low-H₂O Silicic magmas of the Yellowstone hotspot; an experimental study of rhyolite from the Bruneau-Jarbidge eruptive center, central Snake River Plain, USA. *Journal of Petrology* **53**(9), 1837–1866.
- Annen, C. & Sparks, R. S. J. (2002). Effects of repetitive emplacement of basaltic intrusions on thermal evolution and melt generation in the crust. *Earth and Planetary Science Letters* **203**, 937–955.
- Bachmann, O., Dungan, M. A. & Lipman, P. W. (2002). The Fish Canyon magma body, San Juan volcanic field, Colorado: Rejuvenation and eruption of an upper crustal batholith. *Journal of Petrology* **43**, 1469–1503.
- Bacon, C. R. (1989). Crystallization of accessory phases in magmas by local saturation adjacent to phenocrysts. *Geochimica et Cosmochimica Acta* **53**(5), 1055–1066.
- Bacon, C. R. & Lowenstern, J. B. (2005). Late Pleistocene granodiorite source for recycled zircon and phenocrysts in rhyodacite lava at Crater Lake, Oregon. *Earth and Planetary Science Letters* **233**, 277–293.
- Baker, D. R. (1991). Interdiffusion of hydrous dacitic and rhyolitic melts and the efficacy of rhyolite contamination of dacitic enclaves. *Contributions to Mineralogy and Petrology* **106**, 462–473.
- Baker, D. R. & Watson, E. B. (1988). Diffusion of major and trace elements in compositionally-complex Cl- and F-bearing silicate melts. *Journal of Non-Crystalline Solids* **102**, 62–70.
- Bea, F. (2010). Crystallization dynamics of granite magma chambers in the absence of regional stress: multiphysics modeling with natural examples. *Journal of Petrology* **51**, 1541–1569.
- Bea, F. & Montero, P. (2013). Diffusion-induced disturbances of the U–Pb isotope system in pre-magmatic zircon and their influence on SIMS dating. *A numerical study*. *Chemical Geology* **349–350**, 1–17.
- Beard, J. S., Ragland, P. C. & Crawford, M. L. (2005). Reactive bulk assimilation: A model for crust–mantle mixing in silicic magmas. *Geology* **33**, 681–684.
- Bernini, D., Audetat, A., Dolejs, D. & Keppler, H. (2013). Zircon solubility in aqueous fluids at high temperatures and pressures. *Geochimica et Cosmochimica Acta* **119**, 178–187.
- Bindeman, I. N. (2003). Crystal sizes in evolving silicic magma chambers. *Geology* **31**, 367–370.
- Bindeman, I. N. & Simakin, A. G. (2014). Rhyolites—Hard to produce, but easy to recycle and sequester: Integrating microgeochemical observations and numerical models. *Geosphere* **10**(5), 930–957.
- Bindeman, I. N., Fu, B., Kita, N. & Valley, J. W. (2008). Origin and evolution of Yellowstone silicic magmatism based on the ion microprobe analysis of isotopically zoned zircons. *Journal of Petrology* **49**, 163–193.
- Boehnke, P., Watson, E. B., Trail, D., Harrison, T. M. & Schmitt, A. K. (2013). Zircon saturation re-revisited. *Chemical Geology* **351**, 324–334.
- Carley, T. L., Miller, C. F., Wooden, J. L., Bindeman, I. N. & Barth, A. P. (2011). Zircon from historic eruptions in Iceland: reconstructing storage and evolution of silicic magmas. *Mineralogy and Petrology* **102**, 135–161.

- Carrichi, L., Simpson, G. & Schaltegger, U. (2014). Zircons reveal magma fluxes in the Earth's crust. *Nature* **511**, 457–461.
- Carslaw, H. S. & Jaeger, J. C. (1959). *Conduction of Heat in Solids*, 2nd edn. Oxford: Clarendon Press, 510 pp.
- Cavosie, A. J., Quintero, R. R., Radovan, H. A. & Moser, D. E. (2010). A record of ancient cataclysm in modern sand: shock microstructures in detrital minerals from the Vaal River, Vredefort Dome, South Africa. *Geological Society of America Bulletin* **122**, 1960–1980.
- Chamberlain, K. J., Morgan, D. J. & Wilson, C. J. N. (2014). Timescales of mixing and mobilization in the Bishop Tuff magma body: perspectives from diffusion chronometry. *Contributions to Mineralogy and Petrology* doi:10.1007/s00410-014-1034-2.
- Charlier, B. & Zellmer, G. (2000). Some remarks on U–Th mineral ages from igneous rocks with prolonged crystallisation histories. *Earth and Planetary Science Letters* **183**, 457–469.
- Claiborne, L. L., Miller, C. F. & Wooden, J. L. (2010). Trace element composition of igneous zircon: a thermal and compositional record of the accumulation and evolution of a large silicic batholith, Spirit Mountain, Nevada. *Contributions to Mineralogy and Petrology* **160**, 511–531.
- Clemens, J. D. & Vielzeuf, D. (1987). Constraints on melting and magma production in the crust. *Earth and Planetary Science Letters* **86**, 287–306.
- Colón, D. P., Bindeman, I. N., Ellis, B. S., Schmitt, A. K. & Fisher, C. M. (2015). Hydrothermal alteration and melting of the crust during the Columbia River Basalt–Snake River Plain transition and the origin of low- $\delta^{18}\text{O}$ rhyolites of the Central Snake River Plain. *Lithos* **224–225**, 310–323, doi:10.1016/j.lithos.2015.02.022.
- Conte, S. D. & deBoor, C. (1972). *Elementary Numerical Analysis*. New York: McGraw–Hill.
- Cooper, K. M. & Kent, A. J. R. (2014). Rapid remobilization of magmatic crystals kept in cold storage. *Nature* **506**, 480–483.
- Costa, F., Andreatuti, S., Bouvet de Maisonneuve, C. & Pallister, J. S. (2013). Petrological insights into the storage conditions, and magmatic processes that yielded the centennial 2010 Merapi explosive eruption. *Journal of Volcanology and Geothermal Research* **261**, 209–235.
- Courant, R., Friedrichs, K. & Lewy, H. (1928). Über die partiellen Differenzgleichungen der mathematischen Physik. *Mathematische Annalen* **100**(1), 32–74.
- Crank, J. (1975). *The Mathematics of Diffusion*, 2nd edn. Oxford: Oxford University Press, 414 pp.
- Drew, D. L., Bindeman, I. N., Watts, K. E., Schmitt, A. K., Fu, B. & McCurry, M. (2013). Crustal-scale recycling in caldera complexes and rift zones along the Yellowstone hotspot track: O and Hf isotopic evidence in diverse zircons from voluminous rhyolites of the Picabo volcanic field, Idaho. *Earth and Planetary Science Letters* **381**, 63–77.
- Druitt, T. H., Costa F., Deloule E., Dungan, M. & Scaillet, B. (2012). Decadal to monthly timescales of magma transfer and reservoir growth at a caldera volcano. *Nature* **482**, 77–80.
- Dufek, J. & Bergantz, G. W. (2005). Lower crustal magma genesis and preservation: A stochastic framework for the evaluation of basalt–crust interaction. *Journal of Petrology* **46**, 2167–2195.
- Ghiorso, M. S. & Sack, R.O. (1995). Chemical mass-transfer in magmatic processes IV: A revised and internally-consistent thermodynamic model for the interpolation and extrapolation of liquid–solid equilibria in magmatic systems at elevated temperatures and pressures. *Contributions to Mineralogy and Petrology* **119**, 197–212.
- Gualda, G. A. R., Ghiorso, M. S., Lemons, R. V. & Carley, T. L. (2012). Rhyolite–MELTS: A modified calibration of MELTS optimized for silica-rich, fluid-bearing magmatic systems. *Journal of Petrology* **53**, 875–890.
- Hanchar, J. M. & Hoskin, P. W. O. (eds) (2003). Zircon. *Mineralogical Society of America and Geochemical Society, Reviews in Mineralogy and Geochemistry* **53**, 500 pp.
- Harrison, T. M. & Watson, E. B. (1983). Kinetics of zircon dissolution and zirconium diffusion in granitic melts of variable water content. *Contributions to Mineralogy and Petrology* **84**, 66–72.
- Harrison, T. M. & Watson, E. B. (1984). The behavior of apatite during crustal anatexis: equilibrium and kinetic considerations. *Geochimica et Cosmochimica Acta* **48**(7), 1467–1477.
- Harrison, T. M., Watson, E. B. & Aikman, A. K. (2007). Temperature spectra of zircon crystallization in plutonic rocks. *Geology* **35**(7), 635–638.
- Hermann, J. & Rubatto, D. (2009). Accessory phase control on the trace element signature of sediment melts in subduction zones. *Chemical Geology* **265**, 512–526.
- Hildreth, W. (1979). The Bishop Tuff: evidence for the origin of compositional zonation in silicic magma chambers. In: Chapin, C. E. & Elston, W. E. (eds) *Geol Soc Am Spec Pap* **180**, 43–75.
- Holtz, F. (1992). Effects of H₂O on liquidus phase-relations in the haplogranite system at 2 and 5 kbar. *American Mineralogist* **77**, 1223–1241.
- Hoskin, P. W. O. & Schaltegger, U. (2003). The composition of zircon and igneous and metamorphic petrogenesis. In: Hanchar, J. M. & Hoskin, P. W. O. (eds) *Zircon. Mineralogical Society of America and Geochemical Society, Reviews in Mineralogy and Geochemistry* **53**, 27–62.
- Huppert, H. E. & Sparks, R. S. J. (1988). The fluid dynamics of crustal melting by injection of basaltic sills. *Transactions of the Royal Society of Edinburgh, Earth Sciences* **79**, 237–243.
- Kempe, U., Gruner, T., Nasdala, L. & Wolf, D. (2000). Relevance of cathodoluminescence for the interpretation of U–Pb zircon ages, with an example of an application to a study of zircons from the Saxonian Granulite Complex, Germany. In: Pagel, M., Barbin, V., Blanc, P. & Ohnenstetter, D. (eds) *Cathodoluminescence in Geosciences*. Berlin: Springer, pp. 415–455.
- Levich, V. G. (1962). *Physicochemical Hydrodynamics*. Englewood Cliffs, NJ: Prentice–Hall, 700 pp.
- Loewen, M. W. & Bindeman, I. N. (2015). Oxygen isotope and trace element evidence for three-stage petrogenesis of the youngest episode (260–79 ka) of Yellowstone rhyolitic volcanism. *Contributions to Mineralogy and Petrology* doi:10.1007/s00410-015-1189-5.
- Loewen, M. W. & Bindeman, I. N. (2016). Oxygen isotope thermometry reveals high magmatic temperatures and petrogenetic differences between hot-dry Yellowstone/ Snake River Plain and Icelandic rhyolites compared to cold-wet systems. *American Mineralogist* doi:10.2138/am-2016-5591.
- Lundstrom, C. C. (2009). Hypothesis for origin of convergent margin granitoids and Earth's continental crust by thermal migration zone refining. *Geochimica et Cosmochimica Acta* **73**, 5709–5729.
- Miller, C. F., McDowell, S. M. & Mapes, R. W. (2003). Hot and cold granites? Implications of zircon saturation temperatures and preservation of inheritance. *Geology* **31**(6), 529–532.
- Miller, C. F., Furbish, D. J., Walker, B. A., Claiborne, L. L., Koteas, G. C., Bleick, H. A. & Miller, J. S. (2011). Growth of plutons by incremental emplacement of sheets in crystal-rich host: Evidence from Miocene intrusions of the Colorado River region, Nevada, USA. *Tectonophysics* **500**, 65–77.
- Piwinskii, A. J. (1968). Experimental studies of igneous rock series, Central Sierra Nevada Batholith, California. *Journal of Geology* **76**, 548–570.

- Rapp, R. P. & Watson, E. B. (1986). Monazite solubility and dissolution kinetics: implications for the thorium and light rare earth chemistry in felsic magmas. *Contributions to Mineralogy and Petrology* **94**, 304–316.
- Reid, M. R., Vazquez, J. A. & Schmitt, A. K. (2011). Zircon-scale insights into the history of a Supervolcano, Bishop Tuff, Long Valley, California, with implications for the Ti-in-zircon geothermometer. *Contrib. Mineral Petrol* **161**, 293–311.
- Rivera, T. A., Schmitz, M. D., Crowley, J. L. & Storey, M. (2014). Rapid magma evolution constrained by zircon petrochronology and $^{40}\text{Ar}/^{39}\text{Ar}$ sanidine ages for the Huckleberry Ridge Tuff, Yellowstone, USA. *Geology* **42**, 643–646.
- Rubatto, D. & Hermann, J. (2007). Experimental zircon/melt and zircon/garnet trace element partitioning and implications for the geochronology of crustal rocks. *Chemical Geology* **241**, 38–61.
- Rubatto, D., Hermann, J. & Buick, I. S. (2006). Temperature and bulk composition control on the growth of monazite and zircon during low-pressure anatexis (Mount Stafford, Central Australia). *Journal of Petrology* **47**, 1973–1996.
- Rustad, J. (2015). Interaction of rhyolite melts with monazite, xenotime and zircon surfaces. *Contrib Mineral Petrol* **169**, 50–58.
- Ryerson, F. J. & Watson, E. B. (1987). Rutile saturation in magmas: implications for Ti–Nb–Ta depletion in island-arc basalts. *Earth and Planetary Science Letters* **86**, 225–239.
- Schaltegger, U., Brack, P., Ovtcharova, M., Peytcheva, I., Schoene, B., Stracke, A., Marocchi, M. & Bargossi, G. M. (2009). Zircon and titanite recording 1.5 million years of magma accretion, crystallization and initial cooling in a composite pluton (southern Adamello batholith, northern Italy). *Earth and Planetary Science Letters* **286**, 208–218.
- Schmitt, A. K., Perfit, M. R., Rubin, K. H., Stockli, D. F., Smith, M. C., Cotsonika, L. A., Zellmer, G. F., Ridley, W. I. & Lovera, O. M. (2011). Rapid cooling rates at an active mid-ocean ridge from zircon thermochronology. *Earth and Planetary Science Letters* **302**, 349–358.
- Schmitz, M. D. & Schoene, B. (2007). Derivation of isotope ratios, errors, and error correlations for U–Pb geochronology using ^{205}Pb – ^{235}U –(^{233}U)-spiked isotope dilution thermal ionization mass spectrometric data. *Geochemistry, Geophysics, Geosystems* **8**, Q08006, doi:10.1029/2006GC001492.
- Simakin, A. G. & Bindeman, I. N. (2008). Evolution of crystal sizes in the series of dissolution and precipitation events in open magma systems. *Journal of Volcanology and Geothermal Research* **177**(4), 997–1010.
- Simakin, A. G. & Bindeman, I. N. (2012). Remelting in caldera and rift environments and the genesis of hot, ‘recycled’ rhyolites. *Earth and Planetary Science Letters* **337**, 224–235.
- Stelten, M. E., Cooper, K. M., Vazquez, J. A., Calvert, A. T. & Glessner, J. J. G. (2015). Mechanisms and timescales of generating eruptible magmas at Yellowstone Caldera from zircon and sanidine geochronology and geochemistry. *Journal of Petrology* doi:10.1093/petrology/egv047.
- Storm, S., Shane, P., Schmitt, A. K. & Lindsay, J. M. (2011). Contrasting punctuated zircon growth in two syn-erupted rhyolite magmas from Tarawera volcano: Insights to crystal diversity in magmatic systems. *Earth and Planetary Science Letters* **301**, 511–520.
- Trail, D., Watson, E. B. & Tailby, N. D. (2012). Ce and Eu anomalies in zircon as proxies for the oxidation state of magmas. *Geochimica et Cosmochimica Acta* **97**, 70–87.
- Tuttle, O. F. & Bowen, N. (1958). Origin of Granite in the Light of Experimental Studies in the System Ab–Or–Qz–H₂O. *Geological Society of America, Memoirs* **74**.
- Valley, J. W. (2003). Oxygen isotopes in zircon. In: Hanchar, J. M. & Hoskin, P. W. O. (eds) *Zircon. Mineralogical Society of America and Geochemical Society, Reviews in Mineralogy and Geochemistry* **53**, 343–385.
- Vazquez, J. A. & Reid, M. R. (2002). Time scales of magma storage and differentiation of voluminous high-silica rhyolites at Yellowstone caldera, Wyoming. *Contributions to Mineralogy and Petrology* **144**, 274–285.
- Vervoort, J. D. & Patchett, P. J. (1996). Behavior of hafnium and neodymium isotopes in the crust: Constraints from Precambrian crustally derived granites. *Geochimica et Cosmochimica Acta* **60**, 3717–3733.
- Wallace, P., Anderson, A. T. & Davis, A. M. (1999). Gradients in H₂O, CO₂, and exsolved gas in a large-volume silicic magma system; interpreting the record preserved in melt inclusions from Bishop Tuff. *Journal of Geophysical Research* **B104**, 20097–20122.
- Watson, E. B. (1996). Dissolution, growth and survival of zircons during crustal fusion: Kinetic principles, geological models and implications for isotopic inheritance. *Transactions of the Royal Society of Edinburgh, Earth Sciences* **87**, 43–56.
- Watson, E. B. & Harrison, T. M. (1983). Zircon saturation revisited: temperature and compositional effects in a variety of crustal magma types. *Earth and Planetary Science Letters* **64**, 295–304.
- Watson, E. B. & Muller, T. (2009). Non-equilibrium isotopic and elemental fractionation during diffusion-controlled crystal growth under static and dynamic conditions. *Chemical Geology* **267**, 111–124.
- Watts, K. E., Bindeman, I. N. & Schmitt, A. K. (2011). Large-volume rhyolite genesis in caldera complexes of the Snake River Plain: insights from the Kilgore Tuff of the Heise Volcanic Field, Idaho, with comparison to Yellowstone and Bruneau–Jarbridge rhyolites. *Journal of Petrology* **52**(5), 857–890.
- Watts, K. E., Bindeman, I. N. & Schmitt, A. K. (2012). Crystal-scale anatomy of a dying supervolcano: An isotope and geochronology study of individual phenocrysts from voluminous rhyolites of the Yellowstone caldera. *Contributions to Mineralogy and Petrology* **164**, 45–67.
- Wotzlaw, J. F., Bindeman, I. N., Schaltegger, U., Brooks, C. K. & Naslund, H. R. (2012). High-resolution insights into episodes of crystallization, hydrothermal alteration and remelting in the Skaergaard intrusive complex. *Earth and Planetary Science Letters* **355**, 199–212.
- Wotzlaw, J. F., Schaltegger, U., Frick, D. A., Dungan, M. A., Gerdes, A. & Günther, D. (2013). Tracking the evolution of large-volume silicic magma reservoirs from assembly to supereruption. *Geology* **41**, 867–870.
- Wotzlaw, J. F., Bindeman, I. N., Watts, K. E., Schmitt, A. K., Caricchi, L. & Schaltegger, U. (2014). Linking rapid magma reservoir assembly and eruption trigger mechanisms at evolved Yellowstone-type supervolcanoes. *Geology* **42**, 807–810.
- Wotzlaw, J. F., Bindeman, I. N., Stern, R. & Schaltegger, U. (2015). Rapid heterogeneous assembly of multiple magma reservoirs prior to Yellowstone supereruptions. *Nature Scientific Reports* **5**, 14026, doi:10.1038/srep14026.
- Xu, Z. & Zhang, Y. (2009). Zr diffusion in rhyolitic melt during zircon dissolution. American Geophysical Union, Fall Meeting 2009, abstract V43C-2262.
- Zhang, Y. X., Walker, D. & Leshner, C.E. (1989). Diffusive crystal dissolution. *Contributions to Mineralogy and Petrology* **102**, 492–513.
- Zhang, Y. X., Ni, H. & Chen, Y. (2010). Diffusion data in silicate melts. In: Zhang, Y. & Cherniak, D. J. (eds) *Diffusion in Minerals and Melts. Mineralogical Society of America and Geochemical Society, Reviews in Mineralogy and Geochemistry* **72**, 313–408.